Rapid Magnetization Transfer Magnetic Resonance Imaging

Inaugural dissertation

to

be awarded the degree of Dr. sc. med.
presented at
the Faculty of Medicine
of the University of Basel

by

Roya Afshari

from Tuyserkan, Iran

Basel, 2023

Approved by the Faculty of Medicine on application of

Prof. Dr. phil. Oliver Bieri, University of Basel, *primary advisor*

Prof. Dr. med. Cristina Granziera, University of Basel, *secondary advisor*

Prof. Dr. phil. Sebastian Kozerke, ETHZ and University of Zurich, *external expert*

Dr. phil. Francesco Santini, University of Basel, *further advisor*

Basel, 11.04.2023

Prof. Dr. Primo Schär

Dean

Acknowledgement

I would like to express my deepest gratitude to

- Oliver Bieri for his kind and patient mentorship, unwavering support, and profound wisdom. I am humbled and honored to have had him as my supervisor, and I will always cherish the knowledge and insights he imparted on me. Words cannot fully convey the extent of my gratitude toward his trust and confidence in me throughout my PhD.
- Cristina Granziera for her energetic supervision, insightful ideas, and examination of this thesis.
- Sebastian Kozerke for evaluating this thesis as my external expert.
- Francesco Santini for answering my numerous sequence programming questions with patience and expertise, which helped me to overcome many challenges in my research.
- Grzegorz Baumann, for his encouraging and calm guidance which helped me navigate last part of my research with confidence.
- Craig Meyer, Rahel Heule, and Josef Pfeuffer for fruitful and enjoyable collaborations.
- Claudia Weidensteiner, Rahel Heule, Orso Pusterla, Francesco Santini, Santhosh Iyyakkunnel and Jessica Schäper for taking the time to proofread parts of this thesis despite their demanding schedule.

I would like to extend my sincere appreciation to my friends and colleagues from the Radiological Physics group in Basel, Xeni Deligianni, Claudia Weidensteiner, Tanja Hass, Matthias Weigel, Philipp Madorin, Francesco Santini, Grzegorz Baumann, and Orso Pusterla. for creating a warm and safe working environment that made my PhD journey more enjoyable and memorable.

My heartfelt appreciation goes to my fellow PhD candidates, Santhosh Iyyakkunnel and Jessica Schäper, for their invaluable friendship, many German lessons, and virtual meetings, which provided me with much-needed support and encouragement during the pandemic, and their playful teasing that brought some laughter to my hardest days.

My PhD journey would not have been the same without my Iranian friends, particularly Shiva, Mohammad, Sina, Saina, Niloofar, Abtin, Ali, Zeinab, and Mahdi, who have been a constant provider of laughter, inspiration, and hope.

My heart is full of gratitude for my family, Khadijeh, Shamsi, Mohammadreza, Mahsa, Romina, Nane and Baba-Ali, who have always believed in me and my dreams no matter what.

My gratitude knows no bounds for my dear Meisam, whose love and support have carried me through the toughest of times.

Finally, I want to acknowledge my dad, who left this world before I could share more of my happiness with him. His memory has been an undying source of strength for me throughout my PhD journey.

Abstract

Magnetization transfer (MT) imaging provides a contrast reflecting the properties of hydrogen atoms bound to macromolecules in the tissue. These components, which are short-lived in nature, cannot be captured by conventional MRI methods. However, by saturating the magnetization of macromolecules using an off-resonance radio-frequency pulse, a signal intensity drop is induced, enabling the generation of MT contrast. In principle, MT is expressed in two different ways: (a) Magnetization transfer ratio (MTR), which is a semi-quantitative measure, and (b) quantitative magnetization transfer (qMT) which represent quantitative parameters underlying the MT effect. Both methods have demonstrated their usefulness in the diagnosis and prognosis of various pathologies, such as multiple sclerosis (MS). However, the integration of MT imaging into daily clinical practice remains a challenge due to the general long acquisition time of qMT imaging, the transmit field nonuniformities at high field, and the limited signal-to-noise at low fields.

This thesis aims to address these issues by developing fast and robust methodologies for MT imaging at both low (0.55 T) and high (3 T) field strengths. To this end, a fast spiral multi-slice spoiled gradient echo (SPGR) sequence, combined with a low-resolution B_1-mapping for accurate MTR imaging in less than one minute was implemented. The same method was further developed to obtain accurate and easy-to-calculate whole-brain qMT maps within 5 minutes. Moreover, the feasibility of MT imaging at low field was investigated with an MT-sensitized balanced steady-state free precession (bSSFP) sequence, which slightly outperformed the product SPGR in terms of signal-to-noise ratio (SNR). We further demonstrated that an extremely efficient bSSFP-based sequence, termed bSTAR can be extended to MT imaging at low-field with a submillimeter isotropic resolution within the clinically acceptable scan time.

The techniques presented in this thesis facilitate a wider use of MT imaging in clinics for the diagnosis and prognosis of various diseases.

Zusammenfassung

Die Magnetisierungstransfer (MT) Bildgebung liefert einen Kontrast, der die Eigenschaften der an Makromoleküle im Gewebe gebundenen Wasserstoffatomen widerspiegelt. Diese Komponenten, die von Natur aus kurzlebig sind, können mit herkömmlichen MRT-Methoden nicht erfasst werden. Durch Sättigung der Magnetisierung der Makromoleküle mit einem off-resonanten Hochfrequenzpuls wird jedoch ein Abfall der Signalintensität induziert, der die Erzeugung des MT-Kontrasts ermöglicht. In der Praxis wird MT auf zwei verschiedene Arten dargestellt: (a) über das Magnetisierungstransferverhältnis (MTR), ein halbquantitatives Maß, und (b) über quantitativen Magnetisierungstransfer (qMT), der quantitative Parameter darstellt, die dem MT-Effekt zugrunde liegen. Beide Methoden haben ihren Nutzen bei der Diagnose und Prognose verschiedener Pathologien, wie z. B. der Multiplen Sklerose (MS), unter Beweis gestellt. Die Integration der MT-Bildgebung in die tägliche klinische Praxis ist jedoch nach wie vor eine Herausforderung, aufgrund der im Allgemeinen benötigten langen Messzeit, dem ungleichmäßigen Übertragungsfeld bei hohen Feldstärken und dem geringen Signal-Rausch-Verhältnis bei niedrigen Feldstärken.

Diese Arbeit zielt darauf ab, die genannten Probleme durch die Entwicklung schneller und robuster Methoden für die MT-Bildgebung sowohl bei niedrigen (0.55 T) als auch bei hohen (3 T) Feldstärken anzugehen. Zu diesem Zweck wurde eine schnelle Multislice-Spoiled-Gradient-Echo-Sequenz (SPGR) mit spiralförmiger Auslese in Kombination mit einem niedrig auflösenden B1-Mapping für eine genaue MTR-Bildgebung in weniger als einer Minute Messzeit implementiert. Dieselbe Methode wurde weiterentwickelt, um genaue und einfach zu berechnende qMT-Bilder des gesamten Gehirns innerhalb von 5 Minuten zu erhalten. Darüber hinaus wurde die Durchführbarkeit der MT-Bildgebung bei niedrigem Feld mit einer MT-sensibilisierten balanced steady-state free precession (bSSFP) Sequenz untersucht, welche die Produkt SPGR Sequenz in Bezug auf Signal-Rausch-Verhältnis übertraf. Darüber hinaus haben wir gezeigt, dass eine extrem effiziente bSSFP-basierte Sequenz, genannt bSTAR, auf die MT-Bildgebung bei niedrigem Feld mit einer isotropen Auflösung im Submillimeterbereich innerhalb einer klinisch akzeptablen Messzeit erweitert werden kann.

Die in dieser Arbeit vorgestellten Techniken erleichtern den breiteren Einsatz der MT-Bildgebung in Kliniken für die Diagnose und Prognose verschiedener Krankheiten.

Table of Contents

List of Publications

Journal papers

- Afshari R, Bauman G, Bieri O. Magnetization Transfer Ratio Brain Imaging at 0.55T. Submitted to: Magnetic Resonance in Medicine.
- Afshari R, Santini F, Heule R, Meyer CH, Pfeuffer J, Bieri O. Rapid whole-brain quantitative MT imaging. Zeitschrift für Medizinische Physik. 2023 April. https://doi.org/10.1016/j.zemedi.2023.02.005
- Afshari R, Santini F, Heule R, Meyer CH, Pfeuffer J, Bieri O. One-minute whole-brain magnetization transfer ratio imaging with intrinsic B1-correction. Magnetic Resonance in Medicine. 2021 May;85(5):2686-95. https://doi.org/10.1002/mrm.28618

Conference Abstracts

- Afshari R, Bauman G, Bieri O. On the Prospects of Magnetization Transfer Imaging at 0.55 T. ISMRM & SMRT Annual Meeting & Exhibition (London). 2022. E-Poster.
- Afshari R, Bauman G, Bieri O. Submillimeter Whole Brain Magnetization Transfer Ratio Imaging at Low-Field. ESMRMB Annual Scientific Meeting (online). 2021. E-Presentation.
- Afshari R, Santini F, Heule R, Meyer C, Pfeuffer J, Bieri O. Whole-brain B_1-corrected quantitative MT imaging in less than 5 minutes. ISMRM & SMRT Annual Meeting & Exhibition (online). 2021. E-Poster. (ISMRM Merit Award - Magna cum Laude)
- Afshari R, Santini F, Heule R, Meyer C, Pfeuffer J, Bieri O. One-minute whole-brain magnetization transfer ratio imaging with intrinsic B_1-correction. ISMRM & SMRT Annual Meeting & Exhibition (Online). 2020. E-Poster.

List of Abbreviations

ANN	Artificial Neural Network
bSSFP	Balanced Steady-State Free Precession
CW	Continuous Wave
CSF	Cerebrospinal Fluid
FWHM	Full Width at Half Maximum
GRE	Gradient Echo
GM	Grey Matter
MT	Magnetization Transfer
MRI	Magnetic Resonance Imaging
MTI	Magnetization Transfer Imaging
MTR	Magnetization Transfer Ratio
MS	Multiple Sclerosis
NMR	Nuclear Magnetic Resonance
PDw	Proton Density Weighted
P.U.	Percent Unit
qMT	Quantitative Magnetization Transfer
RF	Radio Frequency
SE	Spin Echo
SAR	Specific Absorption Rate
SPGR	Spoiled Gradient Echo
SSFP	Steady-State Free Precession
SNR	Signal-to-Noise Ratio
SPIRiT	Iterative Self-consistent Parallel Imaging Reconstruction Method
TR	Repetition Time
VFA	Variable Flip Angle
WM	White Matter

Chapter 1

Introduction

1.1 Magnetization Transfer Contrast

Magnetic Resonance Imaging (MRI) is a tomographic imaging technique sensitive to the nuclear magnetic resonance (NMR) signal emitted by the excited hydrogen nuclei positioned in a strong magnetic field. In conventional MRI, the physiochemical properties of the tissue such as proton density, longitudinal (T_1) and transverse (T_2, T_2*) relaxation times contribute to the signal formation, and therefore to the image intensity. Conventional MRI typically detects signals only from mobile hydrogen nuclei (water). In contrast to mobile protons, the MRI signal of immobile hydrogen protons (macromolecules) is extremely short-lived with decay times shorter than the smallest echo times possible (around 10 μs) and can thus not be captured by conventional MRI.

Magnetization transfer (MT) was first demonstrated by Wolff and Balaban in the late 1980s introducing a new contrast beyond conventional T_1, T_2 and T_2* weighted imaging (1). Generally, in biological tissue, the source of MT contrast is the exchange of magnetization between mobile hydrogen protons bound to water molecules and immobile hydrogen protons bound to semi-solid macromolecules and membranes. Exchange of magnetization is possible either by direct chemical exchange or by spin-spin interactions (2).

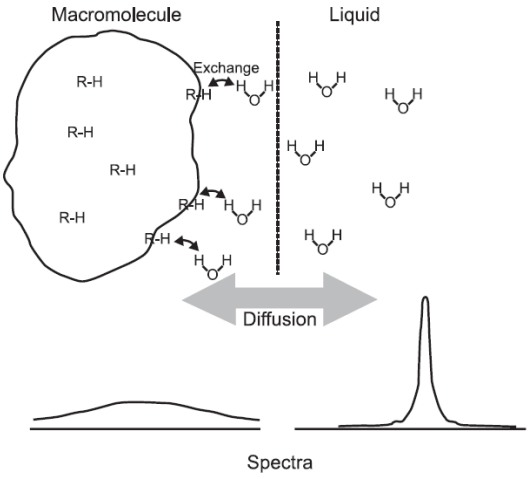

Figure 1.1: Molecular representation for magnetization transfer. Hydrogen atoms attached to macromolecules (R) are relatively immobile and exhibit a short T2 compared to free hydrogen atoms of liquid water. Spins are in constant exchange of magnetization either by chemical or spin-spin interactions. (Figure is from (2))

Typically, free protons have a narrow absorption lineshape and can be excited by an on-resonance radio frequency (RF) pulse. In contrast, immobile protons demonstrate a broad lineshape (as shown in figure 1.2). This offers the possibility of selective saturation of immobile pool without affecting the free pool

using an off-resonance RF pulse which is well away from the central narrow absorption line of the free pool (2,3). The saturated magnetization of the immobile pool is then reflected as a drop of the observed signal from free pool and forms a new contrast called MT. The resulting contrast indirectly describes the contribution of the underlying parameters that govern the transfer of magnetization from immobile protons to free protons.

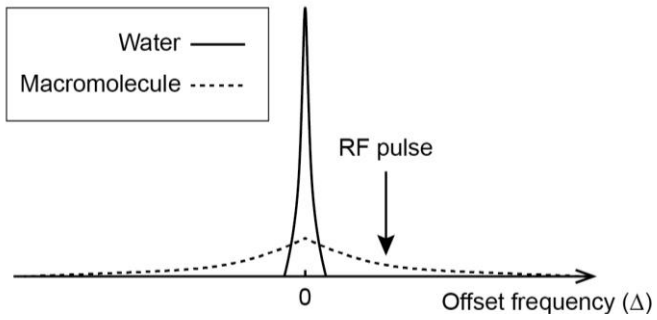

Figure 1.2: Absorption line-shape of water (solid line) and macromolecular pool (dashed line). Macromolecular pool can be selectively saturated by an off-resonance RF pulse away from the central line-shape of water. (Figure is adapted from (3))

1.1.1 Acquisition Strategies

In principle, both spin echo (SE) and gradient echo (GRE) sequences can be used for MT imaging. Barker et al. (4) modified an interleaved dual SE sequence to produce MT images in the clinical setup. To overcome the lengthy acquisition time of SE, a short TR was utilized, which resulted in slight T_1-weighting in the MT-weighted images. In comparison, GRE sequences are faster and can be optimized to avoid T_1-weighting by adjusting the flip angle. As a result, GRE based sequences are currently more popular for MT imaging (5). In general, there are several strategies to induce MT-weighting in GRE sequences. In the following paragraphs, we mention some of the most known methods.

Ideally an MT experiment is performed using an off-resonant continuous wave (CW) irradiation pulse. From its narrow bandwidth, CW irradiation allows complete saturation of the macromolecular pool with minimum direct saturation of the free water pool. It is characterized as a low-amplitude pulse of typical 5 s duration, and an offset frequency of Δ (6). These pulse settings determine the amount of the MT effect. The saturation pulse is limited by the power deposition in the tissue, as expressed by the specific absorption rate (SAR). The implementation of CW experiments in-vivo was however not feasible, as it required hardware modification and was limited by the power deposition restrictions in the clinical workflow.

In contrast, pulsed MT irradiation experiments can be implemented on clinical systems without hardware modification. Pulsed MT imaging, takes advantage of the cumulative saturation caused by a train of short-length (about 10 ms to 30 ms) high-amplitude RF pulses, under the condition that the inter-pulse time is shorter than the spin-lattice and cross relaxation times (7).

On-resonance binomial irradiation is the first proposed pulsed alternative MT method (8–10). The method was based on formation of "transparent pulses" which behave ideally as a zero-degree pulse for long-T_2 species while symmetrically saturate a large range of short-T_2 protons. Nevertheless, on-resonance binomial technique lost popularity to shaped off-resonance pulsed method, as pulse imperfections caused direct saturation and as it offered limited control range over the saturation bandwidth (11,12).

Shaped off-resonance pulsed irradiation, commonly used in MT experiments was first introduced to generate MT-weighted spoiled gradient echo (SPGR) images of the brain in MS patients (5) and has been since successfully incorporated in several other sequences (4,13–15). Generally, narrowband Gaussian-shaped or sinc-shaped off-resonance saturation pulses with a short duration are incorporated into the sequence kernel. Since direct saturation profile of the Gaussian saturation pulses decays faster than sinc-shaped pulses, they are more preferred (13).

Steady-state free precession (SSFP) sequences are a type of rapid GRE sequence in which a steady, residual transverse magnetization is maintained between successive TR intervals. Balanced SSFP (bSSFP) is a specific variation of SSFP where the net gradients in each TR interval are equal to zero. The balanced gradients refocus the SSFP signal components at the exact center of the TR interval as a single echo. Bieri and Scheffler demonstrated that bSSFP is inherently MT-sensitive (16), and that the MT effect can be modulated by adjusting the RF pulse durations (T_{RF}) (17).

In the following sections (1.2 and 1.3), we will introduce two commonly used MT imaging (MTI) techniques, namely the magnetization transfer ratio (MTR) and quantitative magnetization transfer (qMT) and discuss their clinical applications and shortcomings.

1.2 Magnetization Transfer Ratio

Magnetization transfer ratio (MTR) is calculated pixel-by-pixel as subtraction of two proton density weighted (PDw) images: one without (M_0) and one with (M_s) saturation of the immobile proton pool (5). Therefore, the following fraction (see 1. 1) represents the MTR in percent unit ([p.u.]) and indirectly quantifies size of the immobile proton pool in the tissue:

$$MTR = 100 \times (M_0 - M_s)/M_0 \quad 1.1$$

Accordingly, higher signal loss is attributed to the larger size of immobile proton pool in a tissue. For instance, white matter has higher MTR than gray matter, and MTR signal from cerebral spinal fluid is equal to zero. Moreover, it has been shown that MTR is also dependent on two competitive parameters; (i) recovery of magnetization governed by longitudinal relaxation time of the free proton pool, and (ii) loss of magnetization due to its transfer from the free to the bound pool (k_f) (18,19).

1.2.1 Clinical interest of MTR

MTR was initially introduced as a method to detect hidden abnormalities in normal-appearing white matter of the brain (5). Since then, it has become a widely studied in-vivo biomarker for identifying underlying factors causing different abnormalities in the brain, such as brain tumors (20,21), early diagnosis of Alzheimer's disease (22,23), or predominantly for detecting myelin changes in multiple sclerosis (MS) (24–26). Additionally, MTR has been used in head and neck imaging to detect various abnormalities (27,28), and has proven to be useful in cancer studies as well (29–31).

Volumetric histogram analysis is a widely used and valuable approach to evaluate MTR images of the brain. Combining the sensitivity of MTR for both macroscopic and microscopic disease mechanisms with such a volumetric approach, enables the analysis of both focal and diffuse mechanisms underlying various diseases (32–35).

1.3 Quantitative Magnetization Transfer

1.3.1 Two pool model for CW irradiation

Early theory of magnetization exchange was developed based on modified Bloch equations that included additional terms for cross relaxation (36). This theory was referred to as the "two-pool model," the "two-pool Bloch model," or the "binary spin bath model". In this model, macromolecular protons (restricted/immobile pool) are considered in magnetization exchange with free water protons (free pool). After the introduction of MT contrasts to the clinical field (1), Henkelman et al. used a similar set of modified Bloch equations to extract quantitative parameter involved in generation of MT contrasts (6). These set of Bloch equations are generally written as the sum of contribution of pool A and B (see figure 1.3):

$$\frac{dM_{x,f}}{dt} = -\frac{M_{x,f}}{T_{2,f}} - k_f M_{x,f} + k_r M_{x,r} + 2\pi\Delta M_{y,f} \quad 1.2.1$$

$$\frac{dM_{y,f}}{dt} = -\frac{M_{y,f}}{T_{2,f}} - k_f M_{y,f} + k_r M_{y,r} - 2\pi\Delta M_{x,f} + \omega_1(t) M_{z,f} \quad 1.2.2$$

$$\frac{dM_{z,f}}{dt} = R_{1,f}\left(M_{0,f} - M_{z,f}\right) - k_f M_{z,f} + k_r M_{z,r} - \omega_1(t) M_{y,f} \quad 1.2.3$$

$$\frac{dM_{x,r}}{dt} = -\frac{M_{x,r}}{T_{2,r}} - k_r M_{x,r} + k_f M_{x,f} - 2\pi\Delta M_{y,r} \quad 1.2.4$$

$$\frac{dM_{y,r}}{dt} = -\frac{M_{y,r}}{T_{2,r}} - k_r M_{y,r} + k_f M_{y,f} - 2\pi\Delta M_{x,r} + \omega_1(t) M_{z,r} \quad 1.2.5$$

$$\frac{dM_{z,r}}{dt} = R_{1,r}\left(M_{0,r} - M_{z,r}\right) - k_r M_{z,r} + k_f M_{z,f} - \omega_1(t) M_{y,r} \quad 1.2.6$$

where the subscripts r and f represent the restricted (immobile) protons and the free water (mobile) protons, respectively. The magnetization of each pool is described by its longitudinal (M_z) and transverse (M_x, M_y) components. The equilibrium magnetization of the free water pool $M_{0,f}$ is normalized to 1, and the net magnetization of the restricted pool is given as $M_{0,r}$. The $\omega_1(t) = \gamma|B_1(t)|$ corresponds to shape of the CW pulse with constant saturation flip angle of ω_1 , and Δ is the offset frequency of the CW RF pulse. $R_{1,f}$ and $R_{1,r}$ are the rates of longitudinal magnetization recovery ($R_1 = 1/T_1$), in the absence of exchange. Whereas $R_{RF,r}$ and $R_{RF,f}$ represent the saturation terms responsible for longitudinal magnetization loss. The constant R governs the magnetization exchange rate between the two pools; therefore, directional exchanges are defined as pseudo-first order rate constants $k_f = RM_{0,r}$ (forward exchange rate; A→B), and $k_r = RM_{0,f}$ (reverse exchange rate; B →A).

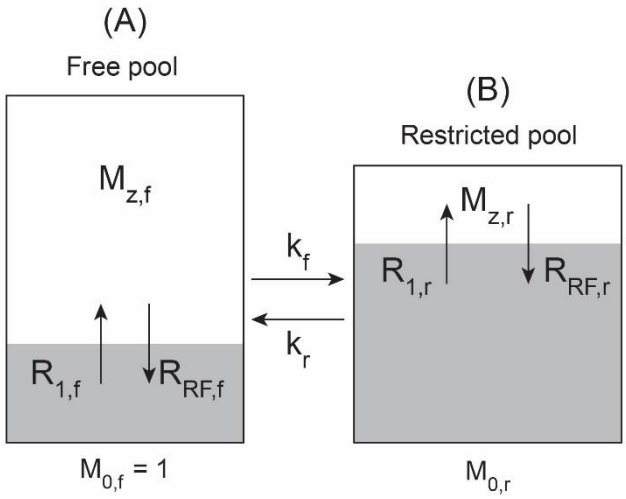

Figure 1.3: The two-pool model (also called the "two-pool Bloch model" or "binary spin bath model") of magnetization transfer. (A) is the 'free' water spin pool, and (B) is the 'restricted' macromolecular spin pool. Saturated spins are shown as grey area. (Figure is adapted from (6))

Due to the very short $T_{2,r}$, the exchange between transverse magnetization components (M_x, M_y) can be neglected. Solving the remaining equations for the steady state condition leads to a closed form solution for the free pool longitudinal magnetization.

$$M_{z,f} = \frac{R_{1,f}R_{1,r} + k_r R_{1,f} + k_f R_{1,r} + R_{RF,r}R_{1,f}}{\left(R_{1,r} + k_r + R_{RF,r}\right)\left(R_{1,f} + k_f + R_{RF,f}\right) - k_f k_r} \qquad \text{Eq. 1.3}$$

where

$$R_{RF,(f,r)} = \frac{\omega_1^2 T_{2,(f,r)}}{1 + (2\pi\Delta T_{2,(f,r)})^2} \qquad \text{Eq. 1.4}$$

Generally, equation 1.4 is proportional to the Lorentzian line-shape. However, the Lorentzian line-shape is not adequate for describing the macromolecular component. Super-Lorentzian line-shape on the other hand was found to be a better approximation for numerical model fitting of the biological tissue, especially in WM (3,37). Assuming that $2\pi\Delta T_{2,r} \gg 1$, Equation 1.4 can be rewritten as

$$M_{z,f} = \frac{M_{0,f}\left[R_{1,r}\left(\frac{k_f}{R_{1,f}}\right) + R_{RF,r} + R_{1,r} + k_r\right]}{\frac{k_f}{R_{1,f}}\left(R_{1,r} + R_{RF,r}\right) + \left[1 + \left(\frac{\omega_1}{2\pi\Delta}\right)^2\left(\frac{1}{R_{1,f}T_{2,f}}\right)\right]\left(R_{RF,r} + R_{1,r} + k_r\right)} \qquad \text{Eq. 1.5}$$

using five model parameters R, $R_{1,r}$, $T_{2,r}$, $\frac{k_f}{R_{1,f}}$, and $\frac{1}{R_{1,f}T_{2,f}}$, where $R_{1,f}$ can be estimated from Equation 1.6 using an independently measured longitudinal relaxation rate ($R_{1,obs}$) when $R \gg \left(R_{1,r} - R_{1,obs}\right)$.

$$R_{1,f} \approx R_{1,obs} - \frac{k_f\left(R_{1,r} - R_{1,obs}\right)}{R_{1,r} - R_{1,obs} + k_r} \qquad \text{Eq. 1.6}$$

Since the exact value of $R_{1,r}$ has little influence on the MT signal, a constant value of $R_{1,r} = 1s^{-1}$ (6) or $R_{1,r} = R_{1,obs}$ (38) can be presumed to further simplify the model.

Ultimately, qMT parameters can be extracted from pixel-by-pixel fitting of Equation 1.5 to the experimental data sampled at multiple CW pulses with different saturation power ω_1 and offset frequency Δ.

1.3.2 Two pool model for pulsed irradiation

For pulsed MT experiments, three main methods were proposed by Sled et al. (39), Yarnykh et al. (40), and Ramani et al. (41), which were based on the adaptation of Henkelman's CW model. Comparison of these methods revealed that the approach proposed by Sled et al. produced the most accurate parameter estimates, albeit at a higher computational cost (42,43). Sled's method involved approximating the pulsed off-resonance irradiation as a rectangular pulse with equivalent average power and a width equal to the full width at half maximum (FWHM) of the saturation RF pulse power $\omega_1^2(t)$. Moreover, the direct saturation effect of the MT pulse on the free pool was assumed to occur instantly and was expressed as an scaling factor, $S_{1,f}$, for the steady state longitudinal magnetization of the free pool. The $S_{1,f}$ was derived from numerical evaluation of a single pool Bloch equation for different $T_{1,f}$ and $T_{2,f}$ values. From adaptation of the CW two-pool model to the described approximations, a closed form equation was derived. Fitting this equation directly to the signal produced qMT parameters, including the macromolecular pool ratio $F = \frac{M_{0,r}}{M_{0,f}} = \frac{k_f}{k_r}$, forward exchange rate k_f, and relaxation times $T_{2,r}$.

1.3.3 Two-pool model for bSSFP

Gloor et al. (44) developed a qMT model for bSSFP by modifying Henkelman's two-pool model. Given all the pulses are played out on-resonance ($\Delta \rightarrow 0$) along the x axis, the set of Bloch equations can be simplified to equations 1.9, leading to a closed-form solution. The qMT parameters were estimated by fitting the model to data points acquired with various RF pulse durations and excitation flip angles.

$$\frac{dM_{y,f}}{dt} = -\frac{M_{y,f}}{T_{2,f}} + \omega_1(t)M_{z,f} \qquad \text{Eq. 1.9.1}$$

$$\frac{dM_{z,f}}{dt} = R_{1,f}\left(M_{0,f} - M_{z,f}\right) - k_f M_{z,f} + k_r M_{z,r} - \omega_1(t)M_{y,f} \qquad \text{Eq. 1.9.2}$$

$$\frac{dM_{z,r}}{dt} = R_{1,r}\left(M_{0,r} - M_{z,r}\right) - k_r M_{z,r} + k_f M_{z,f} - W(\Delta \rightarrow 0, \mathrm{t})(t)M_{z,r} \qquad \text{Eq. 1.9.3}$$

1.3.4 Clinical interest of qMT

Similar to MTR, qMT parameters, specifically the macromolecular pool ratio F, have been demonstrated as a sensitive biomarker for myelin content in the brain (45–47). Compared to myelin measures based on diffusion, relaxation, and susceptibility, F has fewer physiological confounders and is independent of main magnetic field strength (48). Studies have even suggested that F may be a more specific marker of myelin content than MTR (49,50). Moreover, the qMT parameter of forward exchange rate (k_f) has also been shown to be helpful in identifying the effects of mild systemic inflammation in the brain. (51).

1.4 Low-field MTI

The MR scanners that operate at a magnetic field strength of less than 1 T and dubbed low field systems (52) are recently receiving renewed interest given advances in magnet technology, signal detection, data acquisition and processing. One of the primary advantages of low field MRI systems are reduced costs, making them more accessible to smaller clinics and hospitals. They are also considered safer and more comfortable than high field systems as they have reduced SAR and better implant compliance. Low field MRI systems are less likely to produce image artifacts, due to the lower magnetic field strength and the concomitant reduced sensitivity to tissue susceptibility.

However, low field MRI systems have some limitations in terms of image quality and scan times. The lower magnetic field strength leads to less signal-to-noise ratio (SNR), resulting in images with lower resolution and less contrast. Therefore, they may require longer scan times to produce images with acceptable quality, which can be a disadvantage for patient's comfort.

MTI was first applied at low field almost 20 years ago (6,40), but it was limited to a small number of slice acquisitions at a rather long acquisition time. More recently, low-field MTI has been applied to provide fast macromolecular proton fraction mapping (53) although this method still requires a total scan time of 19 minutes.

1.5 Challenges of MT

As previously discussed, both MTR and qMT parameters proved to deliver useful measures of tissue pathology and demonstrated excellent sensitivity to microstructural damage or morphological changes in the brain caused by diseases. Despite the potential benefits of MT for the diagnosis and prognosis of abnormalities, its applicability in day-to-day clinical setting is rather limited, primarily due to the long acquisition times required. Therefore, the aim of this thesis is to develop and test new methodologies that enable fast and accurate whole-brain MT acquisition, both quantitative and semi-quantitative, at various field strengths.

MTR, as a semi-quantitative measure, obtained from two images with and without MT saturation, is sensitive to several sources of variation beyond the exchange rate, such as sequence parameters and main magnetic field. Its dependence on both MT-weighted and non-MT-weighted scans makes it susceptible to motion artifacts. Differences in sequence parameters and vendor-specific characteristics can also lead to variations in MTR measurements. This limits its application in multi-center clinical studies. Furthermore, MTR is highly sensitive to transmit field B_1 inhomogeneity (54). Therefore, it is crucial to minimize these sources of variation to ensure that reliable clinical conclusions are drawn based on MTR.

qMT, on the other hand, provides quantitative MT properties of the tissue, such as F and k_f, that are independent of the sequence parameters and main field strength, thus allowing a more objective assessment of tissue characteristics as compared to MTR. However, MT parameter estimation requires acquisition of several data samples acquired with different MT sensitivities, which can result in a scan time of more than 30-60 minutes for whole-brain coverage. Therefore its application is mostly limited to small-scale or single-slice methodological studies (55). Moreover, B_0 and B_1 field imperfections (56) and intensive computational load hinder qMT application in the day-to-day clinical setting (57). As a result, fast and robust techniques are required for clinically feasible qMT imaging.

The aforementioned challenges have impacted the use of MT imaging at high-fields, which has been the primary focus of researchers in last years, due to the higher achievable signal-to-noise ratio as compared to low field system. On the other hand, the feasibility of MTI at low field strengths is yet to be proven, but of great interest. In fact, recently, low-field systems have gained popularity in the clinical routine due to their higher cost-effectiveness and better safety profile, as well as advancements in hardware and software that allows for improved diagnostic image quality.

Reducing the field strength from 3 T to 0.55 T is expected to result in an SNR reduction by a factor of approximately six. The signal loss could be in theory compensated by increasing the scan time, but it would be unfeasible to prolong the acquisition by a factor of 36 to maintain the image quality. Additionally, the reduction in T_1 values necessitates an efficient acquisition scheme to minimize loss of MTR contrast. Nonetheless, an efficient high-SNR MT imaging protocol that is suitable for low-field imaging has yet to be developed.

1.6 Aim and approach

This thesis addresses three challenges limiting the clinical application of MT: the B_1 sensitivity of both MTR and qMT, the long acquisition time required for qMT imaging, and the feasibility of MT imaging at low field strengths.

In the second chapter (first publication) of this thesis, an attempt is made to exploit speed and robustness of spiral trajectories in combination with an MT-prepared SPGR sequence to generate intrinsically B_1-corrected MTR images within a clinically acceptable scan time and resolution at 3 T. The developed method is assessed for MTR reproducibility through volumetric histogram peak analysis.

The same MT-prepared spiral interleaved SPGR sequence is used in the third chapter (second publication) to address the long acquisition time inherent to quantitative MT methods and derive an efficient acquisition scheme suited for the calculation of quantitative MT parameters. Furthermore, an attempt is made to simplify the complex two-pool model analysis while maintaining the accuracy of the pulsed-MT parameter estimates. The elimination of B_1 and B_0 field inhomogeneity effects on the

calculated qMT parameters is extensively investigated and its necessity for accurate parameter estimation has been explored.

The fourth chapter (third publication) focuses on exploring the feasibility of MT imaging at low fields. To achieve this, a comparative study was conducted with the aim to determine whether bSSFP performs better than product SPGR at low fields as it does at high fields. Next, an efficient bSSFP-based sequence termed bSTAR was used to evaluate whether the signal intensity and MTR can be enhanced at low fields. Overall, the purpose of this chapter was to identify an efficient MT imaging approach that facilitates clinical routine at low fields while avoiding the known limitations that contribute to reduced image quality, such as reduced signal and low-performance gradients.

For all three methods, numerical simulations and in-vivo data of healthy volunteers have been used to show feasibility and superiority of the proposed approaches compared to conventional methods.

Chapter 2

First Publication: One-minute whole-brain magnetization transfer ratio imaging with intrinsic B_1-correction

Status: Published

Magnetic Resonance in Medicine 85, no. 5 (2021): 2686-2695.

DOI: https://doi.org/10.1002/mrm.28618

One-Minute Whole-Brain Magnetization Transfer Ratio Imaging with Intrinsic B_1-Correction

Roya Afshari*[1,2], Francesco Santini[1,2], Rahel Heule[3], Craig H. Meyer[4], Josef Pfeuffer[5], Oliver Bieri[1,2]

[1]Division of Radiological Physics, Department of Radiology, University Hospital Basel, University of Basel, Basel, Switzerland.
[2]Department of Biomedical Engineering, University of Basel, Basel, Switzerland.
[3]High Field Magnetic Resonance, Max Planck Institute for Biological Cybernetics, Tübingen, Germany
[4]Department of Biomedical Engineering, University of Virginia, Charlottesville, Virginia, USA
[5]Siemens Healthcare, Application Development, Erlangen, Germany.

Abstract

Purpose: Magnetization transfer ratio (MTR) histograms are widely used for the assessment of diffuse pathological changes in the brain. For broad clinical application, MTR scans should not only be fast but confounding factors should be minimized for high reproducibility. To this end, a one-minute whole brain spiral MTR method with intrinsic B_1-field correction is introduced.

Methods: A spiral multi-slice spoiled gradient echo sequence with adaptable magnetization transfer (MT) saturation pulses (angle β) is proposed. After a low-resolution single-shot spiral readout and a dummy preparation period, high-resolution images are acquired using an interleaved spiral readout. For whole brain MTR imaging, fifty interleaved slices with three different MT contrasts ($\beta = 0°, 350°, 550°$) together with an intrinsic B_1-field map are recorded in 58.5s on a clinical 3T system. From the three contrasts, two sets of MTR images are derived and used for subsequent B_1 correction, assuming a linear dependency on β. For validation, a binary spin bath model is used.

Results: For the proposed B_1-correction scheme, numerical simulations indicate for brain tissue a decrease of about a factor of ten for the B_1-related bias on MTR. As a result, upon B_1-correction, MTR differences in gray and white matter become markedly accentuated and the reproducibility of MTR histograms from scan-rescan experiments is improved. Furthermore, B_1-corrected MTR histograms show a lower variability for age-matched normal appearing brain tissue.

Conclusion: From its speed and offering intrinsic B_1-correction, the proposed method shows excellent prospects for clinical studies that explore MT-effects based on MTR histogram analysis.

Introduction

Magnetization transfer (MT), reflecting the exchange of magnetization between mobile and bound protons (1), has shown potential for the diagnosis and prognosis of various neurological disorders, such as multiple sclerosis (for a comprehensive overview, c.f. (58)). Frequently, due to time constraints in the clinical workflow, MT effects are condensed into a simple measure in percent unit (pu), termed magnetization transfer ratio (MTR), that can be derived using only two scans performed with and without saturation of the bound pool protons, respectively (5).

MTR imaging has been extensively explored to track morphological changes in brain, such as for the development of myelination in children (59) or within the context of aging (60), for the detection of microstructural damage in normal appearing white matter (5,61–64), or for the detection of a variety of brain disorders, such as Alzheimer's disease (65) and predominantly multiple sclerosis (MS) (5,15,26,33,66). In this context, MTR histograms have proven to be highly indicative of both focal (2) and diffuse tissue damage (2,66–69). Moreover, they allow a distinction of different stages of MS disease (16), a differentiation of MS subgroups (68,69), an estimation of disease burden (32), or a correlation with microscopic changes in gray matter (GM) and white matter (WM) due to aging (70).

It appears evident that a prerequisite for reliable detection of subtle changes in the MTR histogram is a minimization of any confounding factor, such as transmit field (B_1) inhomogeneity or settings of the MT pulse (54). Due to safety limits for power deposition on patients, pulsed rather than continuous wave irradiation is used for MT contrast generation (71,72). This results in a strong but generally incomplete saturation of the bound proton pool. As a result, the observable amount of saturation transfer does thus depend on the off-resonance and the delivered irradiation power, which is locally modulated by B_1 (73,74).

Thus, several approaches were proposed to address B_1-field related variations in MTR values. As a general recommendation, the body coil should be used for transmission (54). Particularly, at high fields, however, object-related B_1-field inhomogeneity becomes more pronounced and appropriate correction of excitation field nonuniformity appears mandatory for accurate estimation of MT effects. To this end, different approaches were suggested to account and correct for B_1-field related MT miscalibrations (73,75–77). Especially, for proton-density weighted spoiled gradient echo (SPGR) MTR acquisitions, a linear correction was found to be adequate (73,76).

For broad clinical translation, MTR scanning should be performed in a reasonable time, ideally without the need for the acquisition of a separate, additional, B_1-field map. In contrast to Cartesian imaging, spiral trajectories might offer a considerable increase in the overall acquisition speed and have found application for rapid tissue quantification, such as MR fingerprinting (78), or for whole brain B_1-field corrected T_1 mapping within less than one minute (79). In this work, we explore the prospects of a one-minute spiral imaging protocol for whole brain MTR imaging with intrinsic B_1-correction.

Methods

Spiral MT sequence

For rapid whole-brain MTR imaging, a prototype interleaved 2D multi-slice SPGR sequence with dual-density spiral-out trajectory (80,81) at a receive bandwidth of 400 kHz was implemented. The spiral trajectory was calibrated in a one-time process using the Tan-Meyer eddy current model (82).

For B_1-correction of MTR, low resolution B_1 mapping was combined with the acquisition of two MTR scans. The two MTR scans were derived from three repetitions of the same sequence using a non-MT-weighted scan and two scans with different off-resonance saturation (angle: β) (Figure 1A). To mitigate possible slice cross-talk and excitation-related MT-effects in neighboring slices, each repetition features two concatenations enabling an interleaved slice excitation scheme for the prototype sequence.

For each slice, a B_1 map was derived from the acquisition of two low-resolution PD-weighted images with nominal flip angles of 90° (PD_1 in Rep1) and 45° (PD_2 in Rep2) using a single-shot spiral readout (Figure 1C). The single-shot contrast image in repetition three is acquired but currently not used for the calculations. A recovery period of about 4 s between repetitions one and two is used to allow for recovery of residual slice cross talk effects in the second single-shot contrast image from the acquisition of the second concatenation in repetition one (Figure 1B and Figure 1C). After the single-shot spiral acquisition, the subsequent interleaved spiral readout preceded a dummy period of about 2 s (MT-preparation, slice excitation and gradients are played out, but no readout is performed) to mitigate transient effects (Figure 1C). The TR was set to 650 ms, offering space for the acquisition of 25 interleaved slices within one concatenation (Figure 1D).

For MT preparation, a Gaussian-shaped off-resonance irradiation pulse of 7.68 ms duration was used (off-resonance $\Delta = 2.2$ kHz). Generally, 3-mm slices with an in-plane resolution of 1.3×1.3 mm^2 (field-of-view: 256×256 mm^2) were acquired using a sinc-shaped RF pulse of 2 ms duration, with a time-bandwidth product of 2.7 and a nominal flip angle α of 35°. Single-shot and interleaved spiral imaging was performed with readout durations of 18.24 ms and 7.88 ms, respectively.

For MTR imaging, 20 spiral interleaves in combination with an acceleration factor R = 2 were used, thus, effectively reducing the number of required spiral interleaves by 50%. The acquisition time for one concatenation was 9.1 s (including the single-shot spiral readout, the dummy preparation period, and the spiral interleaves). The overall acquisition time for the complete scan was 58.5 s (for three repetitions and the recovery).

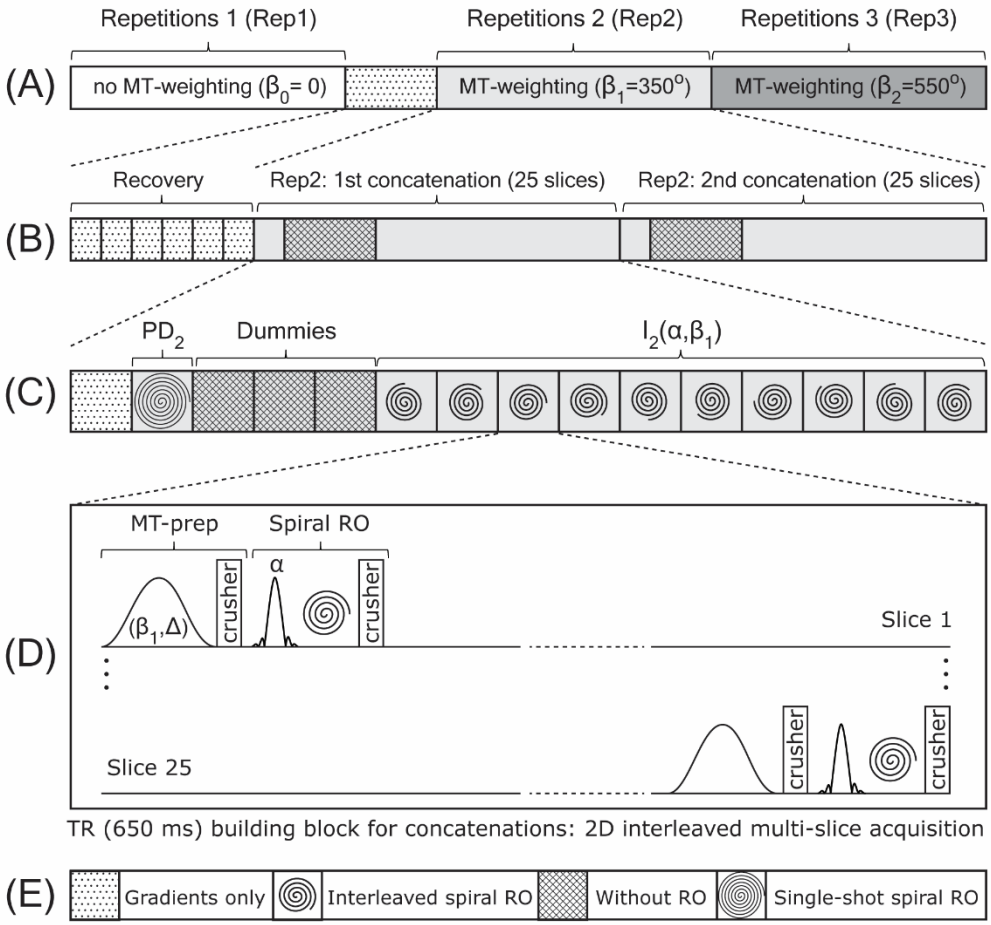

***Figure 1**: Scheme of the prototype 2D interleaved multi-slice spiral MTR imaging approach. (A) three repetitions are acquired with different MT-weightings (β: MT-saturation flip angle). (B) Each repetition features two concatenations with 25 slices each (50 slices in total). Between repetition one and two an additional delay of six TR (about 4 s) allows for full recovery of the concatenations. (C) Each concatenation starts with a single-shot spiral TR, yielding low-resolution PD-weighted images, followed by a dummy period of three TR (about 2 s) without readout (RO), and being terminated by the acquisition of high-resolution PD to mildly T_1-weighted images using a series of N spiral interleaves (N=20). (D) Building block illustrated for one spiral interleave within the 1st concatenation of repetition 2 of the 2D interleaved multi-slice acquisition. The TR is built from 25 interleaved MT-prepared (Δ: off-resonance) slice excitations (flip angle α). (E) legend.*

<u>In-vivo imaging</u>

Imaging was performed on three healthy volunteers (a female at age 28 and two males at ages 31 and 32) at 3T (Magnetom Prisma, Siemens Healthcare, Erlangen, Germany) using a 20-channel receive head coil and approved by the local ethics committee. From a single scan, three repetitions performed

with nominal MT-saturation flip angles of 0°, 350° and 550°. In addition, a standard T_1-weighted scan (MPRAGE (83)) was acquired for brain segmentation.

To test the scan-rescan repeatability and reproducibility, the MTR scan was first run 10 times without breaks and then 10 times with short breaks by taking the volunteer out after every single acquisition (repositioning), and thus forcing a new scanner adjustment. Subsequently, scan-rescan data was co-registered and an MTR histogram analysis was performed for segmented whole-brain, WM and GM. Peak positions were extracted from the segmented GM and WM MTR histograms using non-linear least-squares fitting of a simple Gaussian distribution (54). Subsequently, standard deviation and coefficient of variation (cv: standard deviation over mean of the peak positions) were calculated and boxplots were generated for the assessed peak positions, serving as indicators of repeatability for the scan-rescan experiment.

Image reconstruction, postprocessing and simulations

Spiral image reconstruction was performed online using a spiral version of the iterative self-consistent parallel imaging reconstruction method (SPIRiT) (84). An auto-stop criterion was used, also in case the k-space was fully sampled at the Nyquist rate, to implicitly derive the optimal density compensation function for the gridding algorithm.

Image post-processing and simulation were performed using MATLAB R2019a (The MathWorks, Inc., Natick, MA). For skull stripping, WM and GM segmentation of the T_1-weighted (MPRAGE) images, and co-registration of the derived masks to the spiral-MT image, the standard software package FSL (FMRIB Software Library v6.0, Oxford, UK) was used.

From the signal intensities of the two low-resolution single-shot PD-weighted spiral scans acquired in repetition one and two (PD_1 and PD_2), B_1 can be estimated using (85)

$$B_1 = \zeta \cdot (4/\pi) \cdot \cos^{-1}\left(\frac{PD_1}{2 \cdot PD_2}\right) \quad [1]$$

where ζ = 1.15 takes into account the exact excitation profile and was derived using CoMoTk (86) and is approximately constant within the expected typical B_1 range (variation is less than 1% within B_1 = 0.7 – 1.3). Only the first concatenation was used for B_1 calculation.

Two sets with different MTR contrast can be derived from the interleaved spiral images (I) acquired within the three repetitions with variable MT-saturation flip angles of β_0 = 0°, β_1 = 350° and β_2 = 550° (c.f. Figure 1),

$$MTR_{1,2} = \frac{I_0 - I_{1,2}}{I_0}\ , where\ I_{0,1,2} = I(\beta_{0,1,2}) \quad [2]$$

Assuming a linear dependency of the observable MTR contrast for a reasonable range of flip angle modulations of the MT-preparation pulse, a B_1-corrected MTR image (MTR_c) can be derived using

$$MTR_c = MTR_{avg} + (1 - B_1) \cdot b \cdot \Delta MTR \quad [3]$$

where

$$MTR_{avg} \triangleq (MTR_1 + MTR_2)/2,$$

$$\Delta MTR \triangleq MTR_2 - MTR_1,$$

and

$$b \triangleq 0.5 \cdot (\beta_1 + \beta_2)/(\beta_2 - \beta_1).$$

The linear (first order) correction proposed in Eq. [3] also requires that the B_1-related change in the observable MTR contrast is dominated by the variation of the saturation pulse amplitude only, i.e.

$$\partial_{B_1} MTR(B_1\alpha, B_1\beta) \approx \partial_{B_1} MTR(\alpha, B_1\beta) \quad [4]$$

which appears reasonable for PD to mildly T_1-weighted images (76). To this end, numerical simulations of the binary spin-bath model were performed with MATLAB as described in details elsewhere (7) assuming ideal spoiling for the free pool and using [$M_{0,r}$ = 0.137; $T_{2,r}$ = 12 μs, $R_{1,r}$ = 1 s^{-1}, k_f = 4.3 s^{-1}; R_1 = 1.17] for WM and [$M_{0,r}$ = 0.062; $T_{2,r}$ = 10μs, $R_{1,r}$ = 1s^{-1}, k_f = 1.8 s^{-1}; R_1 = 0.803] for GM at 3T. Observable T_1 tissue parameters for bulk GM (1264 ms) and bulk WM (838 ms) at 3T were taken from (79). For tissues, a super-Lorentzian lineshape was used. Simulations took into account the actual slice excitation profile and were performed with the spiral MT pulse sequence parameters (cf, "spiral MT sequence") until a steady state was reached.

Results

The sequence provided artifact-free images in all volunteers. Example results are shown in Figure 2. As compared to the non-MT weighted images (Figure 2A), MT-weighted images show increasing MT contrast for tissues (and thus incomplete saturation) with increasing MT-saturation flip angles (Figures 2B and 2C). Typically, over the whole brain, nominal MT-saturation flip angles were modulated by the B_1 field by as much as ±30% (cf. Figure 2D). Visual comparison of the images showed a change in the MTR contrast similar in magnitude to the modulation of the B_1 field. As the measured B_1 differences were as large as ±30%, they corresponded to an approximate range of effective MT-saturation flip angles from 350° to 550°.

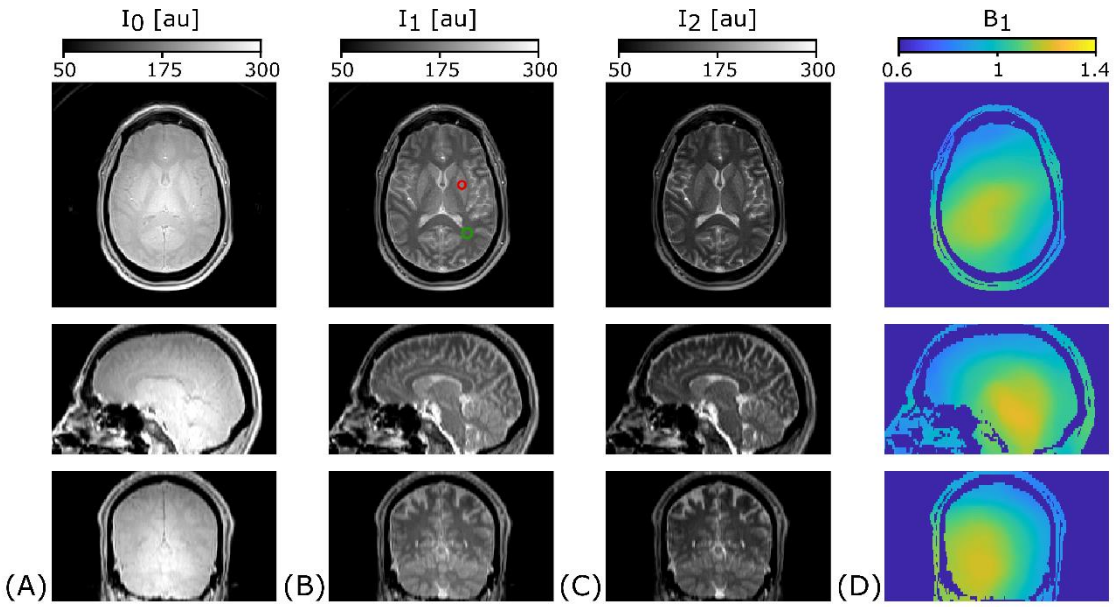

***Figure 2**: Illustrative axial, sagittal and coronal views of: non-MT-weighted images (A), MT-weighted images acquired with an MT-saturation flip angle of 350° (B), MT-weighted images acquired with an MT-saturation flip angle of 550° (C), and a corresponding B1-map (D), derived from PD_1 and PD_2 (c.f. Figure 1).*

The simulated sensitivity of MTR on B_1 is specific for the TR and flip angle used (see 'In-vivo imaging' in the 'Methods' section) and is shown in Figure 3 for GM and WM. Generally, both GM and WM MTR show a slight non-linear dependency on B_1 and increase with increasing B_1. From the two-pool model simulation, the expected B_1-related variation in MTR (for B_1 = 0.7 to B_1 = 1.3) is about 16 – 17 pu (for GM and WM, respectively) and decreases to about 2 pu upon B_1-correction. Overall, the simple linear correction scheme, as proposed in Eq. [3], is able to reduce B_1-related MTR variations by almost a factor of ten.

Average MTR images (MTR_{avg}), B_1-corrected MTR images (MTR_c), as well as absolute difference images are shown in Figure 4. For regions with a B_1 close to 1 no difference is observed, whereas uncorrected MTR_{avg} values are overestimated for the deep parts of the brain, thus predominantly white matter, but underestimated for peripheral regions, such as cortical gray matter. In general, B_1 inhomogeneity leads to up to 8 pu (roughly 16 percent change) changes in MTR values at 3T.

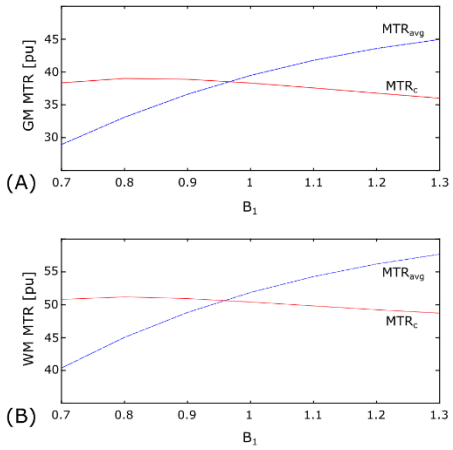

***Figure 3**: Two-pool model simulations of the B_1-dependency of MTR for (A) GM and (B) WM before (MTR_{avg}: dashed blue line) and after correction (MTR_c: solid red line) using Eq [3] (for simulation parameters, see 'Methods' section).*

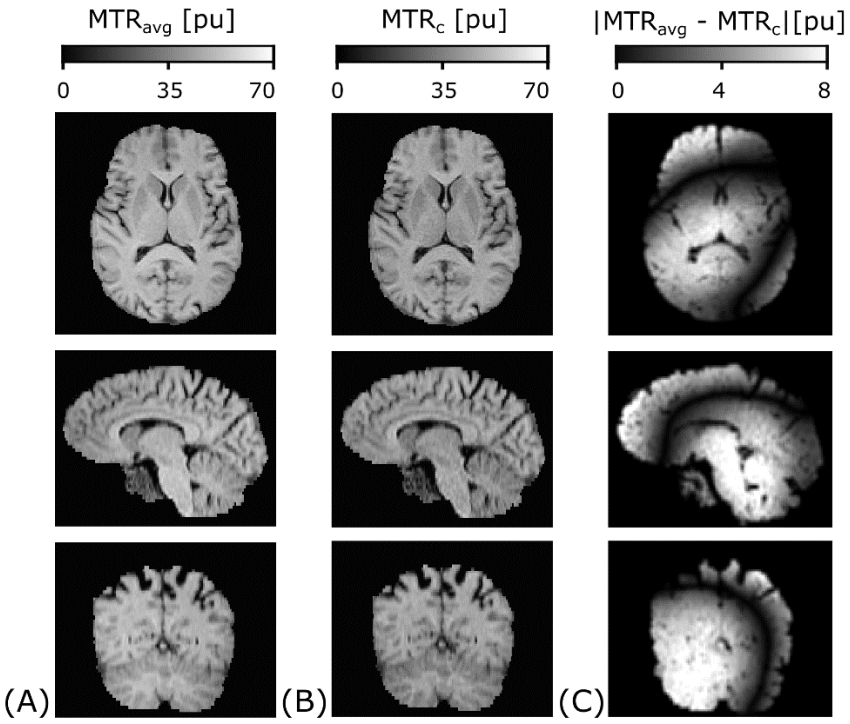

***Figure 4**: Example views in axial, sagittal and coronal orientation of average MTR_{avg} (A) and B_1-corrected MTR_c (B) together with the corresponding absolute difference map (C).*

The overall effect of B_1 correction is further analyzed using MTR histograms (Figure 5). As can be expected from Figure 4, B_1 correction leads to a shift of the whole-brain average MTR_{avg} histogram towards lower values (Figure 5A). In addition, the apparent shoulder in the MTR_{avg} histogram becomes markedly accentuated in the B_1-corrected MTR_c histogram, indicating the presence of (at least) two tissue classes (presumably WM and GM; cf. Figure 4B) with different MT properties that become more separated. Thus, the observed average and B_1-corrected whole brain MTR histograms are further analyzed based on the underlying, segmented, WM and GM (cf. Figures 5B and 5C). The fitting of the Gaussian model resulted in a MTR_{avg} peak at 48.05 pu with a cv = 0.100, and a MTR_c peak at 46.76 pu with a cv is 0.085 for bulk WM. Similarly, for bulk GM, the MTR_{avg} peak was at 39.76 pu with a cv = 0.213, whereas for MTR_c the maximum was at 38.48 pu and the cv was 0.230.

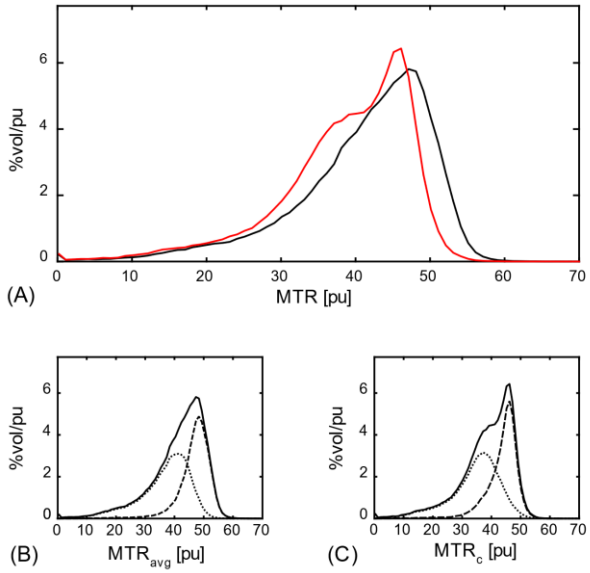

Figure 5*: (A) Whole brain histograms for average (black solid line) and B_1-corrected (red solid line) MTR values of an exemplary subject (B) Average MTR_{avg} histogram (black solid line) segmented into WM (black dashed line) and GM (black dotted line). (C) B_1-corrected MTR_c histogram (black solid line) segmented into WM (black dashed line) and GM (black dotted line).*

The results of the consecutive scan-rescanning are summarized in Figure 6. B_1-correction of MTR did not result in higher peak variability (standard deviation of the WM peak location changed from 0.15 pu to 0.12 pu and for GM from 0.15 pu and 0.09 pu after to B_1 correction), indicating a high stability for the B_1 measurement (Figure 6). While a repositioning of the volunteer and forcing a new scanner adjustment prior to any new MTR scan resulted in a higher variability for the MTR peak positions compared to the consecutive scan-rescan scenario, a lower variability was observed after B_1 correction

(standard deviation of the WM peak location changed from 0.22 pu to 0.14 pu and for GM from 0.21 pu to 0.09 pu after B_1-correction) (Figure 7). This is in line with expectations since a different positioning will generally lead to slightly different B_1-field distributions. As a result, this is expected to become especially accentuated for brain MTR histograms extracted from different volunteers.

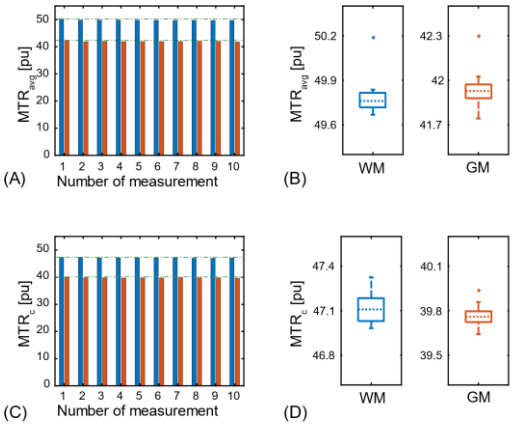

***Figure 6**: Repeatability assessment from scan-rescan experiments (without repositioning) using an MTR histogram peak analysis as shown in Figure 5. (A) Average MTR_{avg} peak values for segmented GM (orange) and WM (blue). (B) Corresponding boxplots, showing median, lower and upper quartiles, as well as the maximum and minimum values. (C) B_1-corrected MTR_c peak values for segmented GM (orange) and WM (blue). (D) Corresponding boxplots, showing median, lower and upper quartiles, as well as the maximum and minimum values.*

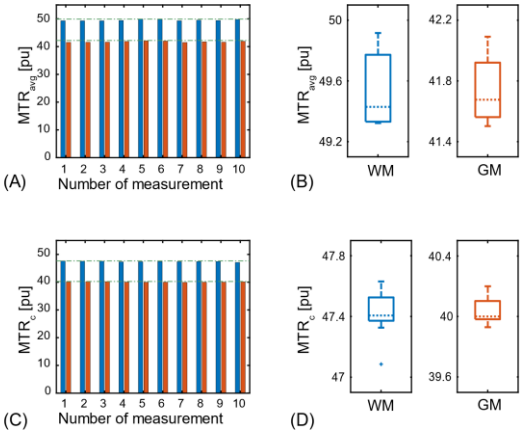

***Figure 7**: Reproducibility assessment from scan-rescan experiments (with repositioning) using an MTR histogram peak analysis as shown in Figure 5. (A) Average MTR_{avg} peak values for segmented GM (orange) and WM (blue). (B) Corresponding boxplots, showing median, lower and upper quartiles, as well as the maximum and minimum values. (C) B_1-corrected MTR_c peak values for segmented GM (orange) and WM (blue). (D) Corresponding boxplots, showing median, lower and upper quartiles, as well as the maximum and minimum values.*

Finally, GM and WM MTR histograms are shown in Figure 8 for three volunteers of highly similar age (30y ± 2y). Average MTR_{avg} histograms for segmented WM and GM are depicted in Figures 8A and 8B. For WM, before B_1 correction the peaks varied within a range of 2.5 pu (46.8 pu to 49.3 pu), which was reduced to 0.9 pu (46.6 pu to 47.5 pu) after correction. Similarly, for GM, before B_1 correction the peaks varied within a range of 2.8 pu (38.7 pu to 41.5 pu), which was reduced to 2.0 pu (38.2 pu to 40.2 pu) after correction. Generally, B_1-correction of MTR values leads to a lower variability for MTR brain histograms, as can be expected for age-matched, normal appearing, brain tissue.

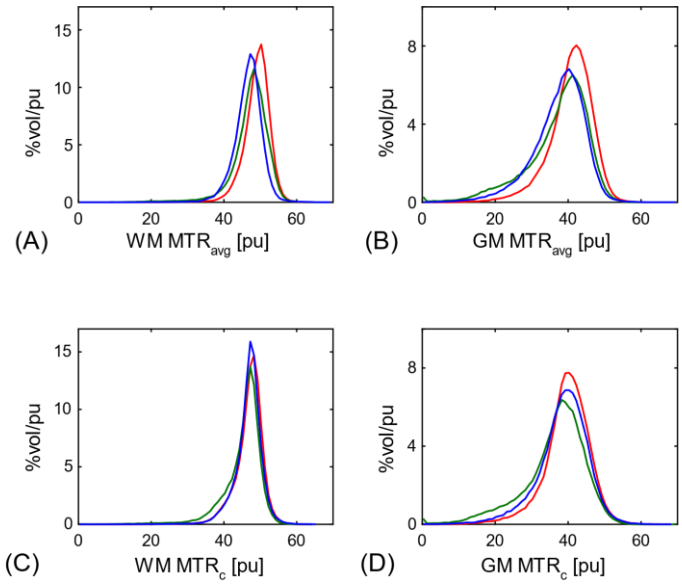

***Figure 8**: Average MTR_{avg} histograms for three age-matched healthy volunteers for segmented WM (A) and GM (B). Corresponding B_1-corrected MTR_c histograms for segmented WM (C) and GM (D).*

Discussion

A fast whole-brain MTR imaging method with intrinsic B_1-correction was introduced. The use of spiral imaging together with iterative parallel image reconstruction enabled an overall acquisition time for B_1-corrected MTR imaging of less than one minute for clinically acceptable resolutions. As a result, MTR scanning has the potential to be performed in the clinical routine setting without any significant workflow or patient throughput sacrifices.

Generally, non-uniform B_1-fields lead to a local variation of the applied MT-saturation power. As a result, even for a homogeneous tissue, any B_1-field variation will lead to a variation in the MT contrast, as long as an incomplete saturation can be presumed. Due to safety restrictions, however, saturation can never be complete, especially for in-vivo human MRI. As a result, all human MTR scans are subjected to B_1-field miscalibrations that become increasingly severe with increasing field strength.

A linear (first order) correction was suggested and implemented to remove the B_1-field related bias in derived MTR values; similar to previous studies and findings (73,75,76). For the suggested protocol, numerical simulations indicate that B_1-related MTR modulations become efficiently reduced. Generally, the quality of B_1-compensation relies on the longitudinal relaxation times and thus on the TR and flip angle settings and is expected to decrease with increasing T_1-weighting. In principle, it appears likely that this could be counterbalanced by a non-linear correction scheme, i.e. using a second order approach, but only at the expense of an overall prolonged scan time (using at least three MT-weighted scans).

In this work, we explored the limits for spiral whole brain MTR imaging in terms of resolution and acquisition speed. Since the proposed linear B_1-correction relies on the acquisition of PD to mildly T_1-weighted images, a rather long TR is required, as preferred by a 2D multi-slice protocol. As a result, scanning is typically performed with high in-plane but low slice resolution. Furthermore, efficient k-space sampling strategies, such as spiral readouts, can only accelerate imaging as long as the signal-to-noise-ratio (SNR) is not limiting. Similarly, resolution can only be increased at the expense of SNR. In summary, it can be expected that with decreasing SNR (and thus with increasing resolution), the proposed spiral imaging approach will offer decreasing benefits in terms of acquisition speed as compared to traditional Cartesian sampling schemes.

Using an integrated B_1-field map acquisition with (almost) no loss of scanning efficiency, we have shown in a scan-rescan experiment that B_1-corrected MTR values as compared to uncorrected ones are not subjected to a higher variability for consecutive scans but are less affected by repositioning and forced scanner readjustments. As a result, B_1-field correction might show added value for single patient follow-up studies, where typically special care is taken that scan-rescans can be performed on the same system (c.f. recommendations from the EURO-MT study, (87)). Our measurements, however, indicate that especially studies based on normative group comparisons, frequently used to assess diffuse pathologic alterations in normal appearing brain tissue, such as for Alzheimer's disease (65,88,89), may profit from the removal of any B_1-field related variations. Generally, B_1-corrected MTR histograms should reveal a lower spread and thus group comparisons should require a smaller cohort size for a given effect size.

Conclusion

In conclusion, we have introduced a one-minute whole brain MTR mapping method, offering intrinsic B_1-field correction. Generally, B_1-field corrected MTR values show a lower variability in scan-rescan experiments as compared to uncorrected ones and might thus be especially beneficial within the context of follow-up studies or for the investigation of diffuse pathological changes based on large patient cohorts. Due to its speed, the proposed method thus not only shows excellent prospects for broad clinical translation but also for application in a variety of clinical studies that explore MT-effects based on a simple MTR analysis.

Chapter 3

Second Publication: Rapid whole-brain quantitative MT imaging

Status: Published

Zeitschrift für Medizinische Physik 2023

DOI: https://doi.org/10.1016/j.zemedi.2023.02.005

Rapid whole-brain quantitative MT imaging

Roya Afshari*[1,2], Francesco Santini[1,3], Rahel Heule[4,5], Craig H. Meyer[6], Josef Pfeuffer[7], Oliver Bieri[1,2]

[1]Division of Radiological Physics, Department of Radiology, University Hospital Basel, Basel, Switzerland.
[2]Department of Biomedical Engineering, University of Basel, Basel, Switzerland.
[3]BAMM group, Department of Biomedical Engineering, University of Basel, Basel, Switzerland.
[4]High Field Magnetic Resonance, Max Planck Institute for Biological Cybernetics, Tübingen, Germany
[5]Department of Biomedical Magnetic Resonance, University of Tübingen, Tübingen, Germany
[6]Department of Biomedical Engineering, University of Virginia, Charlottesville, Virginia, USA
[7]Siemens Healthcare, Application Development, Erlangen, Germany.

Abstract

Purpose: To provide a robust whole brain quantitative magnetization transfer (MT) imaging method that is not limited by long acquisition times.

Methods: Two variants of a spiral 2D interleaved multi-slice spoiled gradient echo (SPGR) sequence are used for rapid quantitative MT imaging of the brain at 3 T. A dual flip angle, steady-state prepared, double-contrast method is used for combined B_1 and-T_1 mapping in combination with a single-contrast MT-prepared acquisition over a range of different saturation flip angles (50 deg to 850 deg) and offset frequencies (1 kHz and 10 kHz). Five sets (containing minimum 6 to maximum 18 scans) with different MT-weightings were acquired. In addition, main magnetic field inhomogeneities (ΔB_0) were measured from two Cartesian low-resolution 2D SPGR scans with different echo times. Quantitative MT model parameters were derived from all sets using a two-pool continuous-wave model analysis, yielding the pool-size ratio, F, their exchange rate, k_f, and their transverse relaxation time, T_{2r}.

Results: Whole-brain quantitative MT imaging was feasible for all sets with total acquisition times ranging from 7:15 min down to 3:15 min. For accurate modeling, B_1-correction was essential for all investigated sets, whereas ΔB_0-correction showed limited bias for the observed maximum off-resonances at 3 T.

Conclusion: The combination of rapid B_1-T_1 mapping and MT-weighted imaging using a 2D multi-slice spiral SPGR research sequence offers excellent prospects for rapid whole brain quantitative MT imaging in the clinical setting.

Introduction

In its simplest and traditional form, magnetization transfer (MT) contrast (1) is quantified from the acquisition of two scans: one without and one with the MT-preparation module (5). The two signals are then condensed within the so-called magnetization transfer ratio (MTR) and a great effort has been undertaken to ensure high reproducibility taking into account intrinsic, as well as possible extrinsic, confounding factors (54). It has, however, also been realized that the phenomenological reduction of a complex tissue system down to a single parameter may lack pathologic specificity making MTR results incomplete and controversial, especially in the brain (90). As a result, biophysical models of MT have been developed that allow the quantitative estimation of the compartmental tissue properties. To this end, two-compartment (or binary) spin-bath models are most commonly considered to yield quantitative MT parameter (qMT) estimates, such as the pool-size ratio of the two compartments, their rate of magnetization exchange, and the compartmental relaxation properties (6,38,39,41). As with any other quantitative MRI method, however, accurate estimation of the underlying tissue model parameters may depend on deviations from the presumed radiofrequency (RF) excitation field (B_1), and inhomogeneities in the main magnetic field (ΔB_0).

Generally, qMT imaging requires multiple MT-weighted measurements and thus prolonged image acquisitions which may prevent widespread clinical use and applicability (38,41). This can, for instance, be addressed by a reduction of the number of free MT model parameters (thus reducing the number of measurements) (38,91).Alternatively, rapid imaging concepts, such as MT-sensitized balanced steady state free precession (bSSFP) (17) or highly efficient k-space sampling schemes, such as MT-sensitized single-shot echo planar imaging (EPI) (14) can be used to reduce the scan time for qMT imaging down to ~10-15 min.

Only recently, a spiral imaging concept was proposed for rapid whole brain MTR imaging with intrinsic B_1-correction within less than one minute (92). The method takes advantage of an MT-weighted multi-slice spiral spoiled gradient echo (SPGR) research sequence offering whole brain coverage for the acquisition of a single MT-weighted volume within 20 s. Notably, the same underlying spiral SPGR research sequence was also suggested for rapid intrinsically B_1-corrected whole brain T_1 mapping in less than one minute (79,81,93). In this work, we thus propose to fuse these two concepts for rapid, whole brain, in-vivo qMT imaging using a two-pool model analysis. We will show that the proposed method allows rapid whole brain qMT imaging in less than typically 5 minutes thus being compatible with the clinical workflow.

Methods

Imaging sequences and image reconstruction

MT-weighted imaging was performed with an interleaved, multi-slice, spiral SPGR research sequence, as described in (79,92). The MT-preparation module had a duration of 19.1 ms and consisted of a 17.92 ms non-selective, unapodized, Gaussian-shaped, radio-frequency saturation pulse with variable frequency offset (Δ) and variable flip angle (β) and crusher gradients. Slice selection was performed with a sinc-shaped RF pulse of 0.6 ms duration and a time-bandwidth-product of 1.6. A flip angle of α = 25 deg and a slice thickness of 3 mm was used. The total acquisition duration of the imaging kernel (including slice selection, spiral readout, and crusher gradients) was 9.75 ms.

For each slice, N_{sp} = 20 spiral interleaves in combination with an acceleration factor of two were used; thus effectively reducing the acquisition to 10 spiral readouts per slice. Data was reconstructed online on the scanner with an in-plane resolution of 1.3×1.3 mm^2 using a spiral version of the "iTerative Self-consistent Parallel Imaging Reconstruction" method (SPIRiT) (84). An auto-stop criterion was used, also when the k-space was fully sampled at the Nyquist rate, to implicitly derive the optimal density compensation function for the gridding algorithm. A single high-resolution MT-weighted volume was reconstructed from the acquisition of N_{sl} = 50 interleaved slices with a repetition time (TR) of 1650 ms (Figure 1). The overall acquisition time for a single MT-weighted whole-brain volume was 19.8 s; including a dummy preparation period of 2×TR (i.e., without readout) to reach the steady state for tissues (see Figure 1A).

In addition, a T_1-map and a low-resolution B_1-map were acquired based on the same spiral research sequence, described in detail in (79). Generally, B_1 field inhomogeneities lead to local deviations from the nominal flip angle, $\alpha_{nom} \rightarrow \alpha_{act} = \zeta_{B1} \cdot \alpha_{nom}$, using a scaling factor ζ_{B1}. Essentially, the same resolution and number of slices were used as for the MT-weighted scans (94). Two scans with optimal variable flip angles (VFA) of 17 deg and 80 deg for a TR of 250 ms were used. The overall acquisition time for the combined B_1 ($\equiv \zeta_{B1}$) and-T_1 mapping was 53 s.

Moreover, a ΔB_0 map (as usual given in Hz via the association $\Delta B_0 \longmapsto \gamma \cdot \Delta B_0$) was derived from the acquisition of two multi-slice GRE volumes with different echo times, TE_1 = 1.45 ms and TE_2 = 1.90 ms. Each acquisition had 50 slices with slice thickness of 3 mm measured with a TR of 180 ms, in-plane resolution of 1.3×1.3 mm^2, and FOV of 256×256 mm^2. The total acquisition time for the ΔB_0 mapping was 22 s.

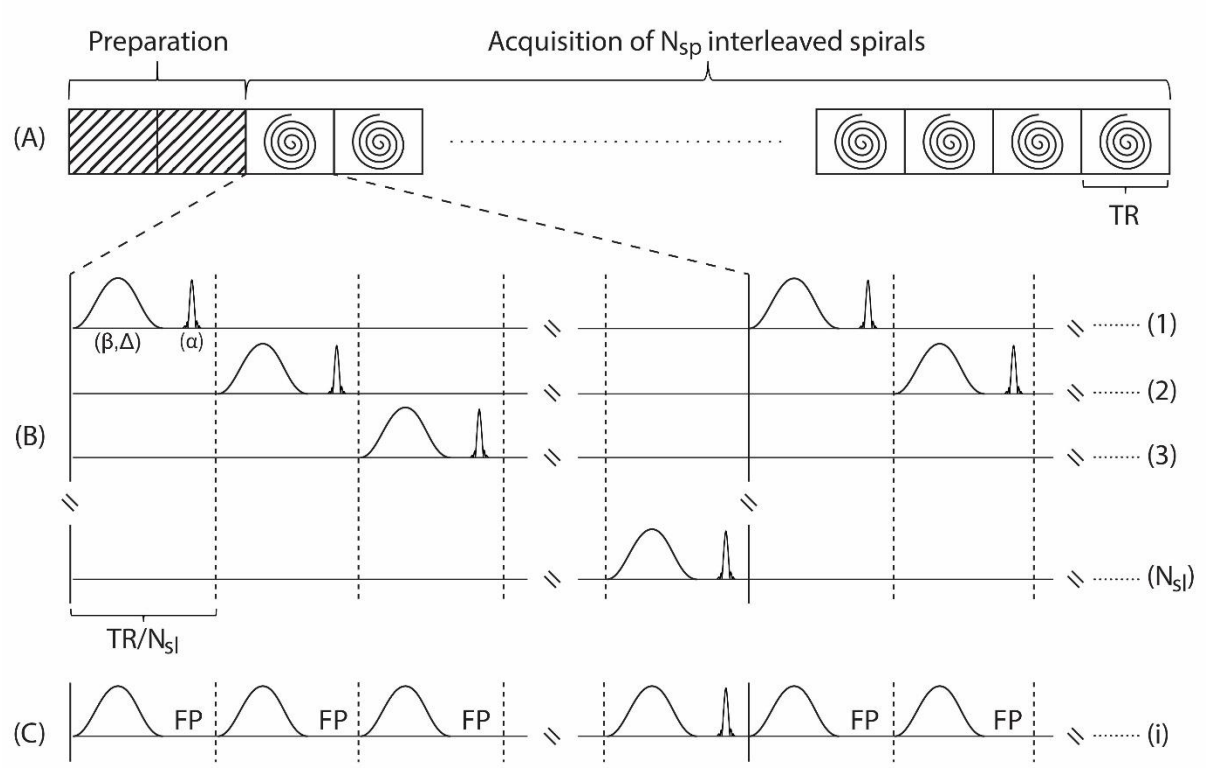

Figure 1: *Scheme of the proposed MT-weighted multi-slice interleaved spiral SPGR sequence. (A) After a dummy preparation period of two TR, data in each slice is sampled by N_{sp} spiral interleaves separated by TR. (B) Within each TR, N_{sl} slices are acquired in an interleaved manner. For each slice, MT preparation with a non-selective gaussian-shaped saturation pulse of variable frequency offset (Δ) and variable flip angle (β) preceded slice excitation with a flip angle (α) using a sinc-shaped excitation pulse. (C) From the interleaved slice acquisition, each slice excitation effectively preceded a train of N_{sl} MT-saturation pulses separated by short free precession (FP) periods.*

MT signal modelling and numerical simulation

From the interleaved slice acquisition (see Figure 1B), pulsed MT-contrast in each slice is generated by a train of N_{sl} MT pulses separated by short free precession periods (see Figure 1C), having an effective duration of 1650 ms (*TR*) and corresponding mean saturation rate $\bar{W}$ (71):

$$\bar{W} = N_{sl}\frac{\pi}{TR}\int_0^{T_{RF}} \omega_1^2(t)\,dt\; G(\Delta) \qquad [1]$$

where $G(\Delta)$ is the absorption line shape, which is assumed to be super-Lorentzian for tissues, and $\bar{W}$ depends on the duration T_{RF} and the shape $\omega_1(t) = \gamma|B_1(t)|$ of the MT pulse.

Consequently, if a fractional saturation of the free pool due to the given train of MT pulses is avoided, the steady state signal S may approximate the situation that is established by a long period of continuous-wave irradiation of the restricted pool protons (see Eq. A5 in ref. (39)):

$$S = c \cdot M_{0,f} \frac{R_{1,r}k_f + R_{1,r}R_{1,f} + R_{1,f}k_r + \bar{W}R_{1,f}}{R_{1,r}R_{1,f} + R_{1,r}k_f + R_{1,f}k_r + \bar{W}R_{1,f} + \bar{W}k_f} \qquad [2]$$

where $M_{0,f}$ is the equilibrium magnetization of the free pool; $R_{1,r}$ and $R_{1,f}$ are the longitudinal relaxation rates of the restricted and of the free pool, respectively; k_f and k_r are the first order exchange rates between the free and the bound pool protons, respectively; and c collects all other parameters, such as coil sensitivities. The exact value of R_{1r} has only a minor influence on MT imaging (39). Following Yarnykh (38), $R_{1,r} = R_{1,obs}$ is chosen, leading to $R_{1,f} = R_{1,obs}$ (cf. Eq. [10] in Ref.(39)). In this work, $R_{1,obs} = R_{1,r} = R_{1,f} = 1/T_1$ is derived from a spiral VFA measurement. Overall, excellent agreement between the spiral VFA method and IR reference measurements were observed (81).

For validation purposes, numerical simulations of the set of coupled Bloch equations including the exchange of longitudinal magnetization in the two-pool model were performed as described in detail, elsewhere (95). Within the context of this work, however, perfect spoiling of transverse magnetization was assumed (note that an interleaved acquisition scheme with a TR of 1650 ms was used) and it was presumed that the offset frequency of the MT-saturation pulse will be chosen large enough to avoid any direct fractional saturation effects of the free pool. For numerical simulation of the steady state signal, we thus proceeded as follows:

MT-pulses were simulated using the coupled Bloch equations, which are reduced to a set of two coupled differential equations for the longitudinal magnetization components,

$$\frac{dM_{z,f}}{dt} = R_{1,f}\left(M_{0,f} - M_{z,f}\right) - k_f M_{z,f} + k_r M_{z,r} \qquad [3a]$$

$$\frac{dM_{z,r}}{dt} = R_{1,r}\left(M_{0,r} - M_{z,r}\right) + k_f M_{z,f} + k_r M_{z,r} - \pi\omega_1^2(t)G(\Delta) \qquad [3b]$$

Note that the train of MT pulses is interleaved by free-precession periods which were simulated by setting ω_1 in Eq. 3b equal to zero. At the end of the pulsed-MT-free-precession train, RF excitation of the free pool occurs, which was assumed to act instantaneously on the longitudinal component of the free pool. The overall succession of MT-pulses, free precession periods, and RF excitation, was repeated until a steady state was reached; which was typically established after two to three repetitions.

A standard ODE solver was used to simulate the time evolution of the longitudinal magnetization components according to Eq. 3 with common white and gray matter MT tissue parameters (96).

Data evaluation

Whole brain voxel-wise B_1 maps, together with B_1-corrected $T_{1,B1}$ and B_1-uncorrected T_1 maps were generated from the two VFA spiral SPGR scans as described elsewhere (79), whereas ΔB_0 maps were derived from the phase factor $e^{-i\gamma\Delta B_0(TE_2-TE_1)}$, relating to the two low-resolution SPGR phase images, acquired with different echo times TE_1 and TE_2. Generally, B_1 effects enter the MT model (cf. Eqs. 1,2) by: (*i*) a modulation of $\omega_1^2 \mapsto \zeta_{B1}^2 \cdot \omega_1^2$, and (*ii*) a correction of the observed $T_1 \to T_{1,B1}$; field inhomogeneities lead to a shift of the off-resonance irradiation frequency $\Delta \mapsto \Delta - \Delta B_0$. Finally, voxel-wise estimates for the pool-size ratio F, k_f, and T_{2r} were derived from a non-linear least-squares (NLLS) fit of Eqs. 1,2 to a set S of MT-weighted signal observations.

The standard software package FSL (FMRIB Software Library v6.0, Oxford, UK) was used for co-registration and skull stripping of the MRI datasets. All other image postprocessing, simulations and visualizations were performed using MATLAB R2019a (The MathWorks, Natick, MA).

In-vivo imaging

Three volunteers were scanned at 3 T (MAGNETOM Prisma, Siemens Healthcare, Erlangen, Germany) using a 20-channel receive head coil. Written informed consent was obtained from participants and measurements were approved by our local ethics committee.

Quite some effort has been undertaken to find optimal sets of MT sampling points that yield robust MT parameter estimates within clinically acceptable scan times (94,97). For 3D scans, about 10 measurements are required (94,97). Similarly, Ramani et al (41) observed a minimum number of about 10 MT measurements using a 2D multi-slice approach with six offset frequencies (Δ) ranging from 1 – 15 kHz using three different saturation flip angles (β). Furthermore, it was observed that at least one point (potentially better two points) with either large Δ or small β (and thus with no MT weighting) should be included (97).

Following Ramani (41), a lower limit of Δ_{min} = 1 kHz was used to mitigate direct saturation effects (cf. Eq. 2), whereas the upper bound for the saturation flip angle was β_{max} = 850 deg due to limits from the specific absorption rate (SAR). The upper limit of Δ_{max} = 10 kHz was configured to maximize the MT signal sensitivity to F and T_{2r} (98). No MT weighting was achieved from using a lower bound of β_{min} = 50 deg. In order to explore a range of 18 down to 6 MT sampling points for subsequent qMT parameter estimation, two base sets of MT-weighted data were acquired:

$$S_1 \coloneqq \{\Delta = 1, 10\ [\text{kHz}] \wedge\ \beta = 50, 150, 250, 350, 450, 550, 650, 750, 850\ [\text{deg}]\}$$

$$S_2 \coloneqq \{\Delta = 1, 10\ [\text{kHz}] \wedge\ \beta = 50, 184, 316, 450, 584, 716, 850\ [\text{deg}]\}$$

From the base sets, the following subsets were synthesized and also analyzed:

$$S_3 \coloneqq \{\Delta = 1, 10\ [\mathrm{kHz}] \wedge\ \beta = 50, 250, 450, 650, 850\ [\mathrm{deg}]\}$$

$$S_4 \coloneqq \{\Delta = 1, 10\ [\mathrm{kHz}] \wedge\ \beta = 50, 316, 584, 850\ [\mathrm{deg}]\}$$

$$S_5 \coloneqq \{\Delta = 1, 10\ [\mathrm{kHz}] \wedge\ \beta = 50, 450, 850\ [\mathrm{deg}]\}$$

The scan times for the base sets S_1 (2 × 9 scans) and S_2 (2 × 7 scans) were 6:00 min and 4:40 min; respectively. The synthetic data sets S_3 (2 × 5 scans), S_4 (2 × 4 scans) and S_5 (2 × 3 scans) have notional scan times of 3:20 min, 2:40 min and 2:00 min, respectively. For qMT imaging, this leads to scan times that range from 7:15 min down to 3:15 min (including 53 s for the two VFA scans for B_1-T_1-mapping and 22 s for the two GRE scans for ΔB_0 mapping).

Results

Figure 2 shows a comparison of the continuous-wave (CW) approximation (Eq. 2) with numerical simulations for white and gray matter using parameter values from (96). Within the range of experimentally applied offset irradiation frequencies (1 and 10 kHz) and saturation flip angles (β = 50 to 850 deg) the CW solution overestimates MT-saturation effects by maximal 1.5% at 10 kHz, and at 1 kHz the maximum relative error amounts to less than 5% for WM and less than 3.5% for GM. In summary, good agreement between the CW solution and the numerical simulations was found.

Figure 3 summarizes in-vivo CW model fitting results (Eqs. [1,2]) for the average signal of two small, presumably homogeneous, regions of interest (ROI1 = 42 pixels, ROI2 = 24 pixels) using data from the 18-samples set S_1. Overall, the fitting residuals indicate appropriate modelling of the data. Upon B_1 and ΔB_0 correction, T_1 and qMT parameter estimates for ROI1 (ΔB_0 = 2.9 Hz, ζ_{B1} = 1.11) change for T_1 from 1182 ms to 873 ms, for F from 14.3±1.2 % to 15.0±1.2 %, for k_f from 3.1±0.4 s^{-1} to 4.2±0.6 s^{-1}, and for T_{2r} from 12.0±0.4 µs to 12.0±0.4 µs. For ROI2 (ΔB_0 = 90 Hz, ζ_{B1} = 0.98), T_1 is changed from 1526 ms to 1597 ms, F is changed from 7.7±0.7 % to 7.4±0.7 %, k_f is changed from 1.9±0.3 s^{-1} to 1.8±0.3 s^{-1}, and T_{2r} is changed from 11.3±0.5 µs to 11.2±0.5 µs. In summary, k_f is most sensitive to and severely affected only by B_1 field miscalibrations, F is affected by both B_1 and ΔB_0 field variations but more strongly by B_1 than ΔB_0 field miscalibrations, whereas the overall bias in T_{2r} appears neglectable.

This finding is further corroborated and summarized in Figure 4, showing the overall bias as introduced by B_1 field miscalibrations only on both T_1 and qMT parameter maps for a single axial slice using again the data from the 18-samples set S_1. The typical B_1 range of about ±25 % at 3 T results in an about two-fold stronger bias in k_f (±50 %), whereas variations in F are about three-fold less (±8 %).

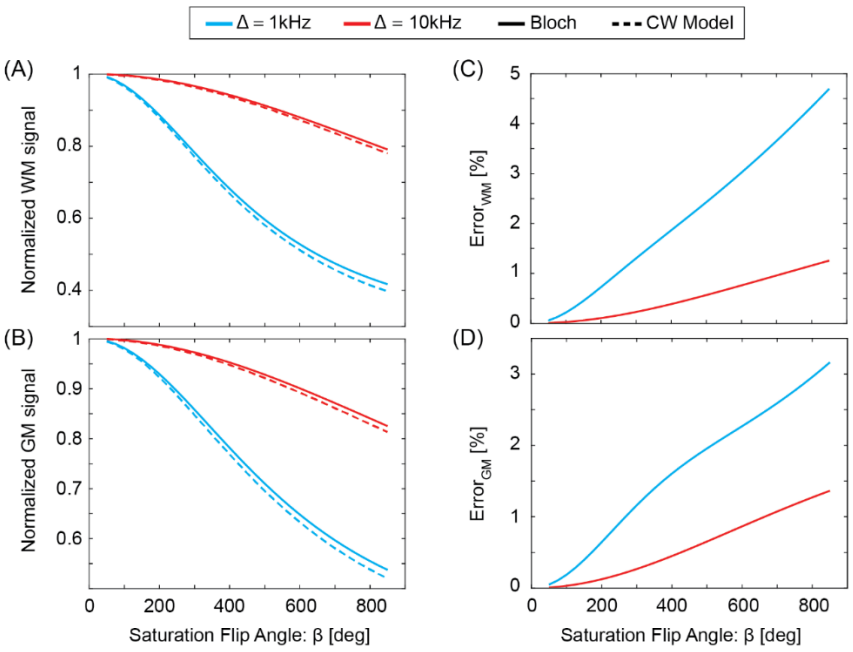

Figure 2: *Bloch simulation (solid line) versus CW two-pool model predictions (Eq. 2, dashed line) for typical MT parameter values at 3 T for (A) white matter (F = 13.7 %, k_f = 4.3 s^{-1}, $R_{1,f}$ = 1.17 s^{-1}, T_{2r} = 12 µs), (B) gray matter (F = 6.2 %, k_f = 1.8 s^{-1}, $R_{1,f}$ = 0.8 s^{-1}, T_{2r} = 10 µs), and their relative difference (C, D) as a function of the saturation flip angle beta at two different offset irradiation frequencies.*

Generally, T_{2r} estimates are not affected by B_1. This is in contrast to ΔB_0 field variations where the maximum observed local off-resonances near the nasal cavity in the order of about +100 Hz lead to local variations in F by a few percent (less than about -3 %) and to overall changes in T_{2r} by less than about 1 %. The forward exchange rate, k_f, is unaffected (see Figure 5 for the assessment of ΔB_0-field miscalibrations on qMT parameter maps).

Figures 3, 4 and 5 were derived using the 18-samples set S_1. In Figure 6, the effect of reduced sample sizes (and thus shortened scan times) on qMT parameter estimation is shown. Generally, qMT parameter maps show no marked fitting failures, even for the 6-samples set S_5. As can be expected, however, the uncertainty in the parameter estimates increases with decreasing number of samples: for a ROI in WM (cf. Figure 6), F and k_f estimates change from 16.3±1.1 % in set S_1 to 16.2±2.1 % in the 10-samples set S_3 to 15.2±5.2 % for the 6-samples set S_5, and from 3.7±0.4 s^{-1} in S_1 to 3.8±0.8 s^{-1} in S_3 to 4.2±2.6 s^{-1} in S_5, respectively. Overall, a similar trend is observed for T_{2r} and similar observations were made for gray matter.

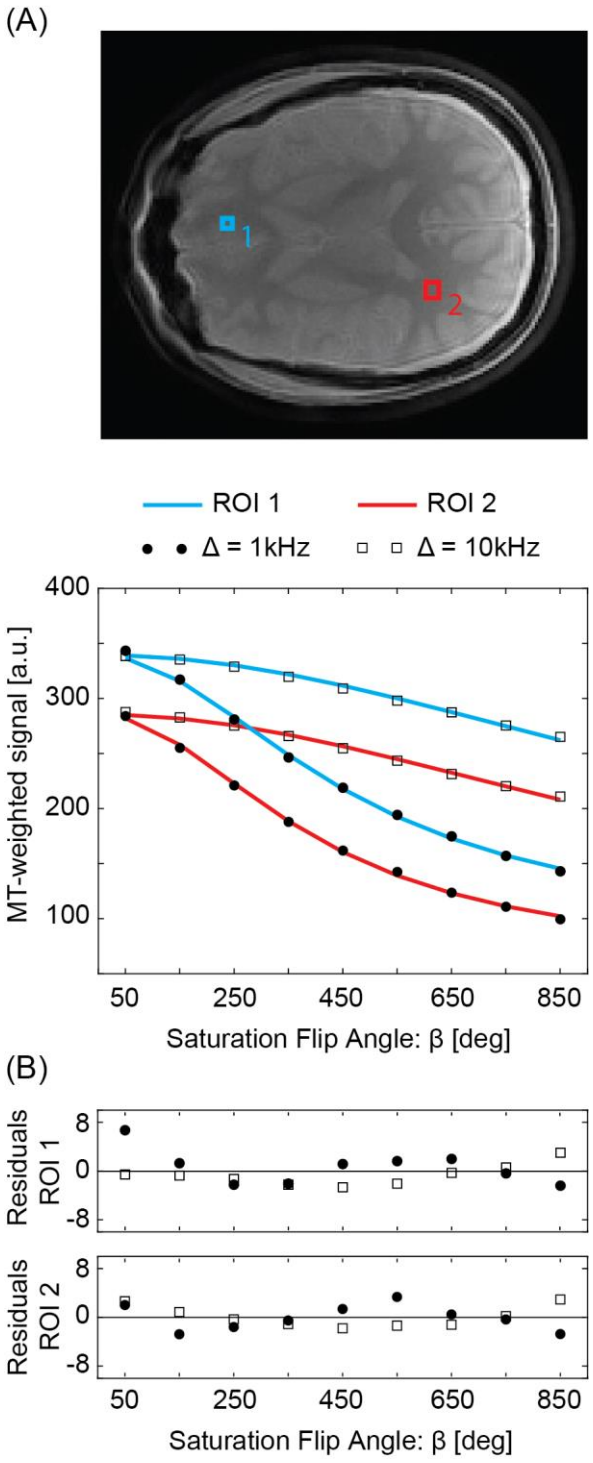

Figure 3: *(A) In-vivo CW two-pool model analysis (solid line) of MT-weighted signals from set S_1 for two regions of interest, located in cortical brain tissue (ROI1, blue box, ΔB_0 =2.9 Hz, ζ_{B1} =1.11) and in the white matter (ROI2, red box, ΔB_0 =90 Hz, ζ_{B1} =0.98). Square dots correspond to regional average signals from the MT-weighted images acquired with an offset frequency of Δ = 10 kHz, whereas round dots are representing regional average signals from MT-weighted images acquired with Δ = 1 kHz. (B) Fitting residuals.*

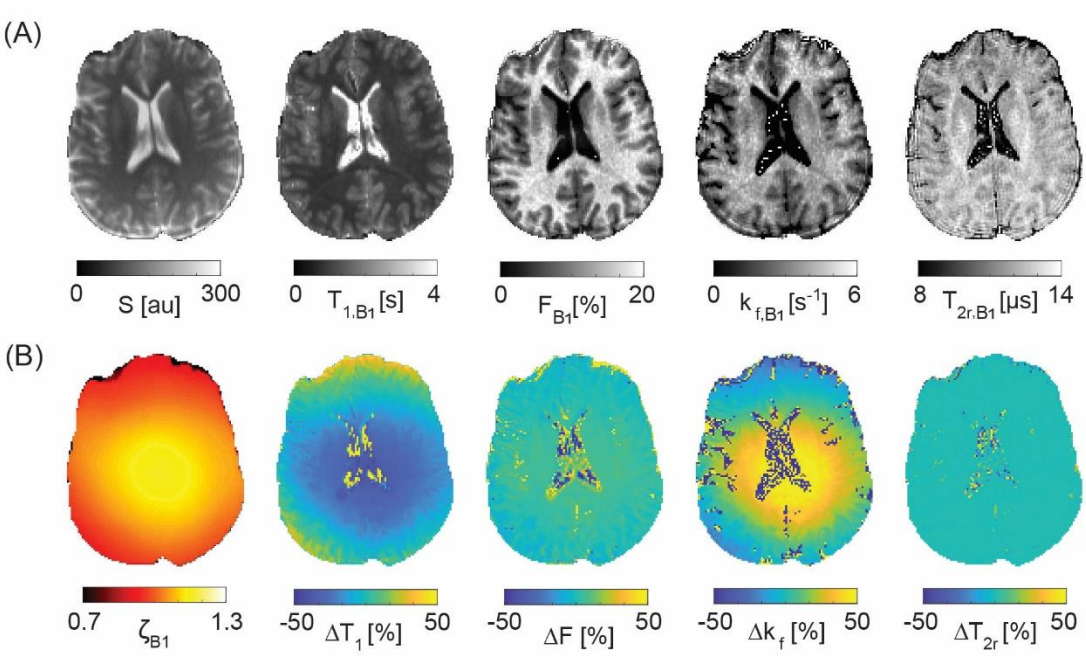

Figure 4: *B_1 bias on qMT model parameters. (A) B_1-corrected $T_{1,B1}$, F_{B1}, $k_{f,B1}$, and $T_{2r,B1}$ parameter maps. (B) B_1-map together with its relative contribution to uncorrected T_1, F, k_f, and T_{2r} parameter estimates.*

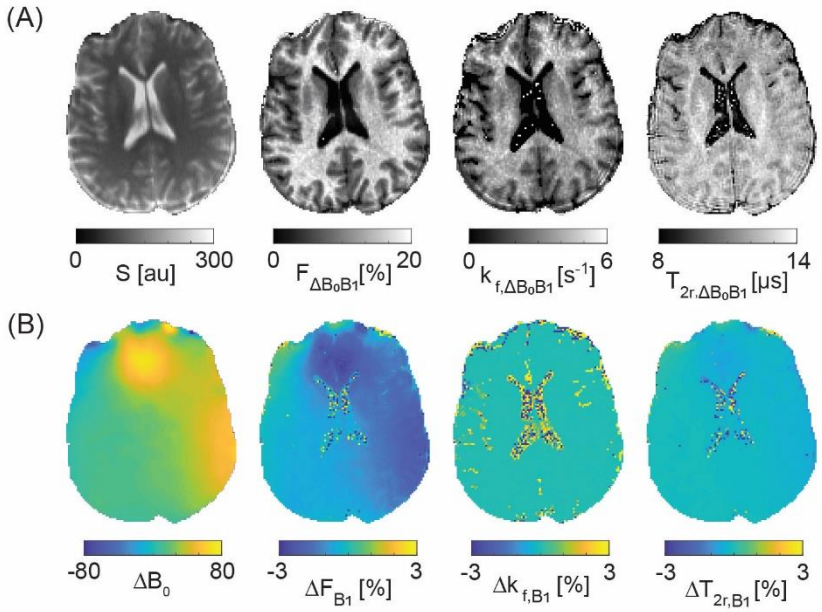

Figure 5: *ΔB_0 bias on B_1-corrected qMT model parameters. (A) ΔB_0-B_1-corrected $F_{\Delta B0B1}$, $k_{f,\Delta B0B1}$ and $T_{2r,\Delta B0B1}$ parameter maps. (B) ΔB_0-map together with its relative contribution to B_1-corrected F_{B1}, $k_{f,B1}$ and $T_{2r,B1}$ parameter estimates.*

Discussion

Generally, qMT parameter mapping requires a set of measurements with different MT-weighting and might thus suffer from over-lengthy scan time requirements in the clinical setting. One obvious strategy to reduce scan time is to reduce the number of MT sampling points and state-of-the-art methods typically require about a minimum of 10 sampling points (94,97). Alternatively, efficient sequences that offer short repetition times, such as bSSFP, can be used to reduce the overall scan time (17). Ideally, however, efficient signal acquisition is combined with a low number of sampling points. To this end, in this work, rapid whole brain qMT imaging was explored using an interleaved multi-slice spiral research sequence at 3 T for combined B_1 and T_1 mapping, as well as for the acquisition of a set of MT-weighted signals with different saturation powers and off-resonances. Due to the interleaved multi-slice acquisition, a simple two-compartment CW MT model could be used to model the data. Without ΔB_0 correction, the total scan time of the investigated B_1-corrected qMT protocols ranges from 6:53 min for the 18-samples set down to 4:13 min for the 10-samples set and finally down to 2:53 min for the 6-samples set, yielding 50 slices with a resolution of $1.3\times1.3\times3.0$ mm^3 for T_1, F, k_f and T_{2r}.

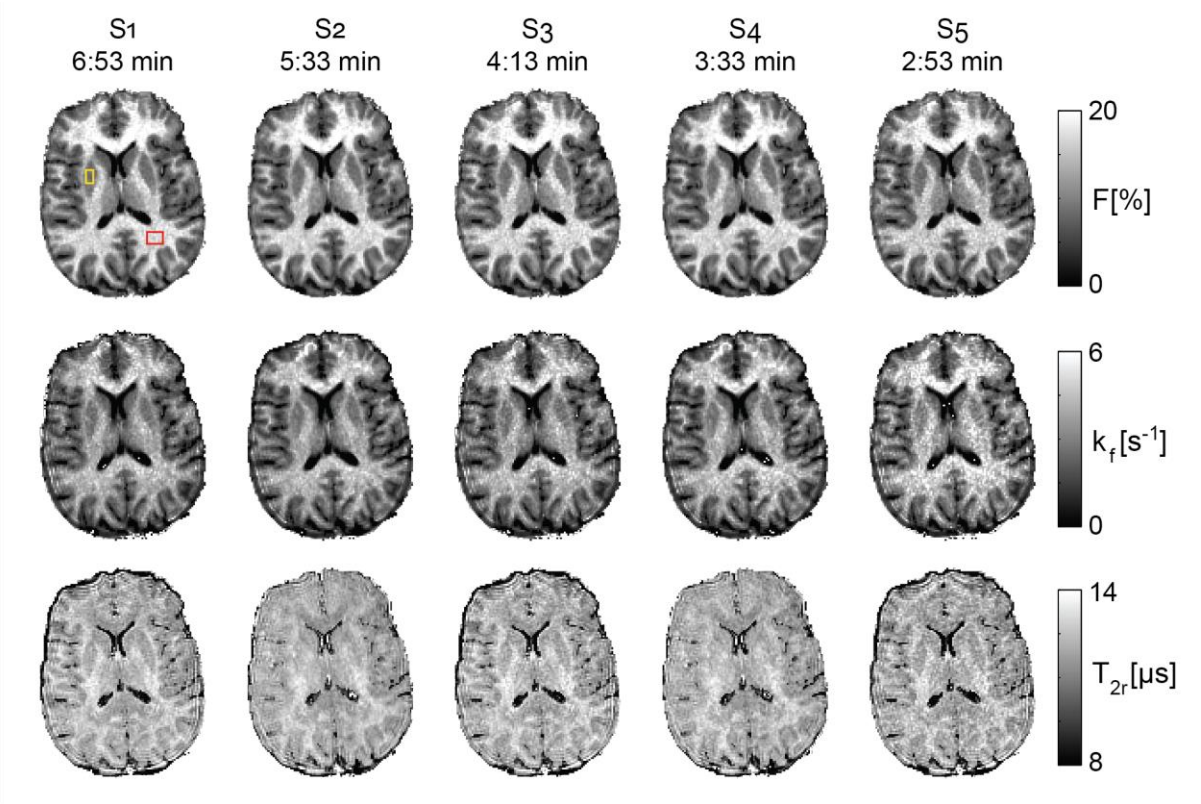

Figure 6: *Effect of sampling point reduction on B_1-corrected qMT parameter estimates.*

Conventional qMT methods use sampling schemes covering a broad range of off-resonances (Δ) at a rather limited number of MT saturation powers (β) (40,41,95). In this work, MT contrast was explored

using a broad range of saturation powers measured at two off-resonances. The latter approach was preferred since conventional methods include low off-resonances (Δ < 1kHz) but Eq. [2] does not account for direct saturation effects. Thus, MT saturation cannot be explored at low off-resonance frequencies. No such restriction, however, applies for the MT saturation power. Moreover, a different signal model is used and it is a priori unclear whether conventional optimal sampling schemes apply here as well.

Overall, no systematic investigation was performed to find the optimal {β,Δ} sampling pattern for a given number of measurements. Thus, different {β,Δ} patterns might be found that even lead to more robust parameter estimates. The 6-point sampling pattern, however, embraces 3 MT saturation powers at two offset frequencies and comes close to the minimal number of scans required (94), indicating a reasonable choice of the sampling pattern. The 10-point sampling scheme together with the combined B_1-T_1 mapping can be performed in less than 5 minutes. Overall, estimated MT parameters were well within the range of what was previously reported (95).

In contrast to related work (56), a higher B_1 bias is observed for F upon using B_1 uncorrected VFA T_1 values (for the settings used here, about three-fold). Consequently, appropriate B_1 correction appears mandatory but requires no extra scan time using the proposed rapid dual-contrast VFA approach (79). This is in contrast to ΔB_0, where the typical maximum bias on F is limited to a few percent and is negligible for all other qMT parameter estimates. Thus, the bias in F from ΔB_0 is on the order of the uncertainty of the measurement, especially for measurements using 10 or less sampling points. Thus, whether ΔB_0 correction needs to be performed depends on the desired accuracy for the qMT parameter estimates, as well as whether the additional required 22 s needs to be spent or not.

Conclusion

A fast qMT imaging method is proposed based on two variants of an interleaved multi-slice spiral research sequence at 3 T. B_1-correction was mandatory for appropriate MT parameter estimation while the overall effect of ΔB_0 can be neglected. The 10-point MT-weighted sampling scheme together with the B_1-T_1 acquisition offers whole brain qMT imaging with clinically relevant resolutions in less than 5 minutes and thus offers excellent prospects for widespread clinical translation and use.

Chapter 4

Third Publication: Magnetization transfer ratio brain imaging at 0.55 T

A modified version of this work is submitted to Magnetic Resonance in Medicine

Magnetization Transfer Ratio Brain Imaging at 0.55T

Roya Afshari*[1,2], Grzegorz Bauman[1,2], Oliver Bieri[1,2]

[1]Department of Radiology, Division of Radiological Physics, University Hospital Basel, Basel, Switzerland.

[2]Department of Biomedical Engineering, University of Basel, Basel, Switzerland.

Abstract

Purpose: To provide a fast high-resolution magnetization transfer (MT) imaging method based on half-radial double-echo bSSFP-sequence (bSTAR) at 0.55 T

Methods: MT-prepared spoiled gradient echo (SPGR) was compared to MT-sensitized balanced steady state free precession (bSSFP) for magnetization transfer ratio (MTR) imaging at 0.55 T using simulations and measurements. The total scan time for MTR imaging was fixed to 5 minutes for both. MT-weighted and non-MT-weighted MRI was performed with an isotropic resolution of 1.5 mm. In addition, an MT-sensitized bSTAR was evaluated offering high sequence efficiency at low field. The reproducibility of MTR MRI with bSTAR was assessed using a histogram peak analysis of twelve consecutive scan-rescan experiments.

Results: At low field, bSSFP MRI of the brain was essentially artifact-free. For 3D MTR imaging, both SPGR-MT and bSSFP-MT offered similar performance. The limited sequence efficiency of bSSFP-MT, however, can be overcome by bSTAR, offering high-resolution MTR MRI with a nominal resolution of 0.87 mm isotropic of the brain within 5 minutes with values comparable to those reported at high field and showing excellent reproducibility.

Conclusion: At low field, a double-echo half-radial bSSFP-based approach, known as bSTAR, produces reliable sub-millimeter isotropic MTR maps of the brain with acquisition times comparable to those of high-field methods.

Introduction

Magnetization transfer (MT) was first demonstrated by Wolff and Balaban in the late 1980s introducing a new contrast beyond conventional T1, T2 and T2* weighted imaging (1) and has found wide-spread application to assess neurological disorders, such as tumors (20,21), Alzheimer's disease (22,23,89,99), and multiple sclerosis (2,25,100,101), or to monitor brain developmental processes (102,103).

The most commonly used method for MT imaging is based on spoiled gradient echo (SPGR) techniques. In this approach, additional off-resonance radio-frequency (RF) irradiation pulses are played out at every repetition time (TR) interval with a high flip angle to induce a strong saturation in the macromolecular pool protons (7,71,87). Upon magnetization exchange processes, saturation is transferred to mobile protons, leading to a prominent and observable signal loss, generating the MT contrast. It is evident that the need for such MT-preparation modules will lower the overall sequence efficiency. In contrast, balanced steady-state free precession (bSSFP) has demonstrated high sensitivity to MT effects (16) that can be modulated by a simple adaptation of the duration of the RF pulses used for excitation (17). As a result, no special MT-preparation modules are required with bSSFP. It has been shown that at high field, 3D bSSFP-MT offers a three to about four times increase in the signal-to-noise ratio (SNR) for magnetization transfer ratio (MTR) imaging of the brain as compared to contemporary 2D SPGR-MT protocols (104). Brain MRI with bSSFP, however, can be hampered in regions of prominent susceptibility variations, such as near the nasal cavities especially at higher field strengths, leading to prominent signal drops, so called banding artifacts (105).

At low field, such as 0.55 T, susceptibility-related field inhomogeneities are considerably reduced, and bSSFP has shown excellent prospects for a wide range of clinical applications (106–109). Obviously, MT imaging of the brain with bSSFP will no longer be challenged by the presence of severe off-resonance artifacts. As a result, following the observations at high field, bSSFP-MT imaging can be expected to represent the ideal choice to perform MTR imaging of the brain at low field. In general, however, longitudinal relaxation (T_1) will also be enhanced at low field (110,111), thus affecting not only the steady state of SPGR and bSSFP sequences, but also the amount of MT-related saturation transfer effects that can be imprinted on the steady state signal. Moreover, at 0.55 T the overall SNR will be considerably reduced, and it is thus questionable whether MTR imaging of the brain can be performed with similar sensitivity and quality as compared to high field.

In this work, we analyze and compare the prospects of 3D volumetric MTR imaging of the brain with isotropic resolution at low field using either SPGR-MT or bSSFP-MT.

Methods

MT imaging

MRI was performed on a commercially available 0.55 T low-field MR-system offering 25 mT/m maximum gradient amplitude and 40 mT/m/ms maximum gradient slew rate (MAGNETOM Free.Max, Siemens Healthineers, Erlangen, Germany). The 12-channel head coil was used for signal reception. Written informed consent was obtained from participants and measurements were approved by our local ethics committee. Three healthy volunteers were scanned (two females and one male with average age of 31.3 years) using a product 3D spoiled gradient echo (SPGR) sequence (87), a custom 3D balanced steady state free precession (bSSFP) sequence (44), and a half-radial dual-echo bSSFP sequence, termed bSTAR (112).

For MT weighting, the product SPGR sequence used a Gaussian-shaped non-selective RF pulse of 7.68 ms duration, played out with an off-resonance of 1500 Hz and a flip angle of 500°. The custom bSSFP and bSTAR sequence used a short non-selective RF excitation pulse of 140 µs duration to generate MT-weighting. Non-MT-weighted imaging with bSSFP and bSTAR was performed with a non-selective RF excitation pulse of 1400 µs and 1800 µs duration, respectively.

For SPGR, imaging was performed with a bandwidth (BW) of 110 Hz/Px and a TE / TR of 5.86 ms / 23 ms (sequence efficiency: $\eta = (BW \cdot TR)^{-1} \sim 40$ %). A field of view (FOV) of 240 × 240 × 240 mm^3 and a matrix size of 160 × 160 × 160 was used yielding an isotropic resolution of 1.5 mm. The acquisition time was 2:46 min for one scan. Six pairs of MT-weighted and non-MT-weighted SPGR scans were acquired with flip angles of 5°, 10°, 15°, 20°, 25°, and 30°.

For bSSFP, MT-weighted imaging was performed with a bandwidth of 868 Hz/px and a TE / TR of 2.15 ms / 4.3 ms (sequence efficiency: $\eta \sim 27$ %). The same FOV and matrix size was used as with SPGR, but with a phase oversampling of 9% to fine tune the overall acquisition time of bSSFP MT-weighted scans averaged five times to the acquisition time of one single SPGR scan. Non-MT-weighted bSSFP imaging was performed with a bandwidth of 919 Hz/px, a TE / TR of 2.75 ms / 5.5 ms (sequence efficiency: $\eta \sim 20$ %) and a phase oversampling of 6 % for bSSFP scans with four averages. Four pairs of MT and non-MT-weighted bSSFP scans were acquired for flip angles of 30°, 40°, 50°, and 60°.

The bSTAR sequence employs a simple bSSFP-kernel with a non-selective RF excitation, a single bipolar gradient for image encoding, and one single ADC spanning the entire length of the bipolar gradient. The two echoes are sampled with center-out and center-in half-radial projections, following an Archimedean spiral trajectory. More technical details about the pulse sequence can be found in (112). Brain MRI with bSTAR was performed with a flip angle of 40°, using 775 Hz/px bandwidth, 40'000 radial half-projections, 208 samples per half-projection for a FOV of 256×256×256 mm^3. MT-weighted images were produced with TE1 / TE2 / TR of 0.10 ms / 2.62 ms / 2.9 ms (sequence efficiency:

$\eta \sim 89$ %); non-MT-weighted with TE1 / TE2 / TR of 0.93 ms / 3.49 ms / 4.5 ms (sequence efficiency: $\eta \sim 57$ %). The acquisition times were 1:57 and 3:01 min for the MT-weighted and the non-MT-weighted bSTAR scans, respectively.

Data from the bSTAR scans were reconstructed off-line to its nominal isotropic resolution of 0.87 mm, as well as to lower resolutions of 1 mm and 1.5 mm, using a GPU accelerated compressed sensing reconstruction with a fast iterative shrinkage-thresholding algorithm (FISTA)(113). The reconstruction time of a single dataset with a reconstruction matrix 320^3 took approximately 50 seconds using 10 FISTA iterations. The in-house developed software for image reconstruction was written in C++ (GNU Compiler Collection 12.2 64-bit on Linux operating system) and CUDA Toolkit 12.0 (NVIDIA Corp., Santa Clara, CA). The reconstruction workstation was equipped with 2x Epyc 7502 CPU (AMD Inc. Santa Clara, CA) and Quadro RTX 8000 GPU (NVIDIA Corp.).

Data evaluation

MTR contrast was calculated from using two acquisitions (5): one without (S) and one with (S_{MT}) the MT-saturation according to

$$MTR = 100 \times (S - S_{MT})/S \qquad [1]$$

and reported in percent unit ([p.u.]).

For a comparison between SPGR-MT and bSSFP-MT, we computed average SNR values for MTR images based on the "difference method" (114), as follows:

From two identical and consecutive SPGR (or bSSFP) scans, a third image volume was derived by taking the difference between the two recorded image volumes. A region-of-interest (ROIs) was placed in the frontal white matter (WM) and noise was estimated from the difference image. Since the same bandwidth and TR was used for all SPGR measurements, noise was estimated from two consecutive non-MT-weighted SPGR acquisitions with a flip angle of 30° and considered to be constant for all SPGR scans. Due to different bandwidths and repetition times used with bSSFP, noise estimation was performed independently for MT-weighed and non-MT-weighted bSSFP acquisitions at flip angle of 40°. The SNR of MTR was then calculated as the ratio of the ROI's average MTR to its standard deviation of noise (as given and measured by the difference method). Finally, the mean and standard deviation of the resulting average SNR of MTR were calculated over all volunteers.

To assess reproducibility, pairs of MT-weighted and non-MT-weighted bSTAR scans were acquired twelve times. The volunteers were repositioned inside the MR-scanner prior to each consecutive scan. Subsequently, MTR histogram analysis of the segmented WM and gray matter (GM) was performed for each MTR image. Histogram peak positions were extracted from bulk GM and WM using non-

linear least-square fitting of a simple Gaussian distribution (54). Box plots were generated for the assessed peak positions, serving as indicators of reproducibility for the scan–rescan experiment.

Skull-stripping and WM and GM segmentation was performed using a standard MPRAGE scan and the results were co-registered to the bSTAR images. The standard software package FSL (FMRIB Software Library v6.0, Oxford, UK) was used for segmentation of the MRI datasets.

Numerical Simulations

For SPGR, a numerical simulation of the two-pool model for MT was performed (6). A standard ODE solver was used to retrieve the time evolution of the magnetization from the set of coupled ordinary differential equations (assuming ideal spoiling of reminiscent transverse magnetization); as described in detail elsewhere (95). For the simulation, the same SPGR-MT sequence timings, and MT pulse settings were used as for imaging (for details, cf section 'MT Imaging).

For bSSFP, MT effects were simulated at on-resonance and based on the analytical two-pool bSSFP model; as described in detail elsewhere (see Eq. 10 in ref. (44)). For the simulation, the same bSSFP sequence and RF pulse settings were used as for the imaging (for details, cf. section 'MT Imaging').

For the two-pool model, the following white matter brain tissue parameters were assumed: F = 15.8 %, k_f = 4.9 s^{-1}, $T_{2,r}$ = 12 µs, $R_{1,r} = R_{1,f}$ (44) with field dependent relaxation times: $T_{1,f}$ = 493 ms, $T_{2,f}$ = 89 ms at 0.55 T, and $T_{1,f}$ = 900 ms, $T_{2,f}$ = 50 ms at 3T. (44,111,115,116). A super-Lorentzian line shape with $G(\Delta \rightarrow 0) = 1.4 \times 10^{-5}$ s^{-1} was assumed for bSSFP.

Monte Carlo simulations were performed to simulate the SNR of MTR imaging as per Eq. [1]. For SPGR-MT imaging, a noise level of n_{SPGR} = 0.005 [M_0] (where M_0 is the equilibrium magnetization) was assumed for both scans; that is without and with MT-weighting. The SNR of MTR for SPGR was simulated as a function of the flip angle and finally normalized to its maximum value. For bSSFP-MT, the noise level was adjusted to the difference in sampling time per unit time, i.e., the sequences bandwidth (*BW*) per unit time, according to

$$\frac{n_{bSSFP}}{n_{SPGR}} = \sqrt{\frac{TR_{bSSFP}}{TR_{SPGR}} \cdot \frac{BW_{SPGR}}{BW_{bSSFP}}} \qquad [2]$$

yielding n_{bSSFP} = 0.006 [M_0] for the MT-weighted bSSFP scan and n_{bSSFP} = 0.007 [M_0] for the non-MT-weighted bSSFP scan. Finally, the SNR of bSSFP-MTR was divided by the maximum value of the SNR of SPGR-MTR.

Simulations, and all other image postprocessing and visualizations were performed using MATLAB R2019a (The MathWorks, Natick, MA).

Results

Numerical simulations of both MT-weighted and non-MT-weighted, white matter SPGR and bSSFP signals are shown in Figure 1 at 0.55 T and 3 T as a function of excitation flip angle. As can be expected, the shortening of the T_1 relaxation time with decreasing main magnetic field leads to an increase in the steady state signal for the SPGR (Figure 1A) and bSSFP (Figure 1B) without MT-weighting. Similarly, the MT-weighted steady state is increased for both methods as a result of reduced persistent MT saturation transfer effects in the liquid pool protons due to enhanced re-polarization (see Figures 1A and 1B). As a result, MTR for SPGR is monotonically increasing with decreasing flip angle, reaching its maximum in the limit of zero flip angles and thus in the limit of zero steady state (Figure 2A), whereas MTR for bSSFP exhibits a pronounced maximum for flip angles that also yield close-to-maximum steady state values (Figure 2B). SNR for SPGR-MTR maximizes for flip angles $\alpha \sim 10° – 15°$ (Figure 2C), and thus with reduced MTR values as compared to the limit of $\alpha \to 0$, whereas SNR for bSSFP-MTR maximizes around its maximum MTR value (Figure 2D). Overall, both methods show a similar SNR performance at low field; with a small advantage for bSSFP (predicted SNR gain of 13 %).

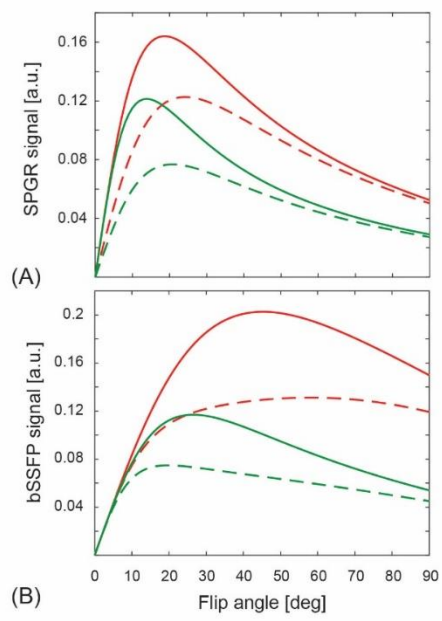

Figure 1: *Simulated MT-weighted (dashed line) and non-MT-weighted (solid line) signal from (A) SPGR and (B) bSSFP for typical white matter values at 0.55 T (red line), and 3 T (green line) as a function of excitation flip angle.*

The results of SPGR-MT imaging are collected in Figure 3 for a range of flip angles covering both the expected maximum MTR and the expected maximum SNR for MTR imaging (see Figure 2). The predicted monotonical decrease in the MTR values with increasing flip angles is apparent. Similarly, a strong modulation of the non-MT-weighted and the MT-weighted SPGR signals is observed, as expected; with a pronounced signal drop as the flip angle approaches zero. This is in contrast to the signal modulations, as observed for bSSFP (Figure 4), around its expected maximum MTR and its expected maximum SNR for MTR imaging. Visually, as imaging is performed around the steady state maximum (Figures 1B and 1D), no pronounced dependence on the flip angle setting is apparent neither

in the MT-weighted and non-MT-weighted bSSFP images, nor in the corresponding MTR image. Generally, due to mitigated susceptibility-related off-resonances at low-field, bSSFP imaging is essentially free of banding artefacts.

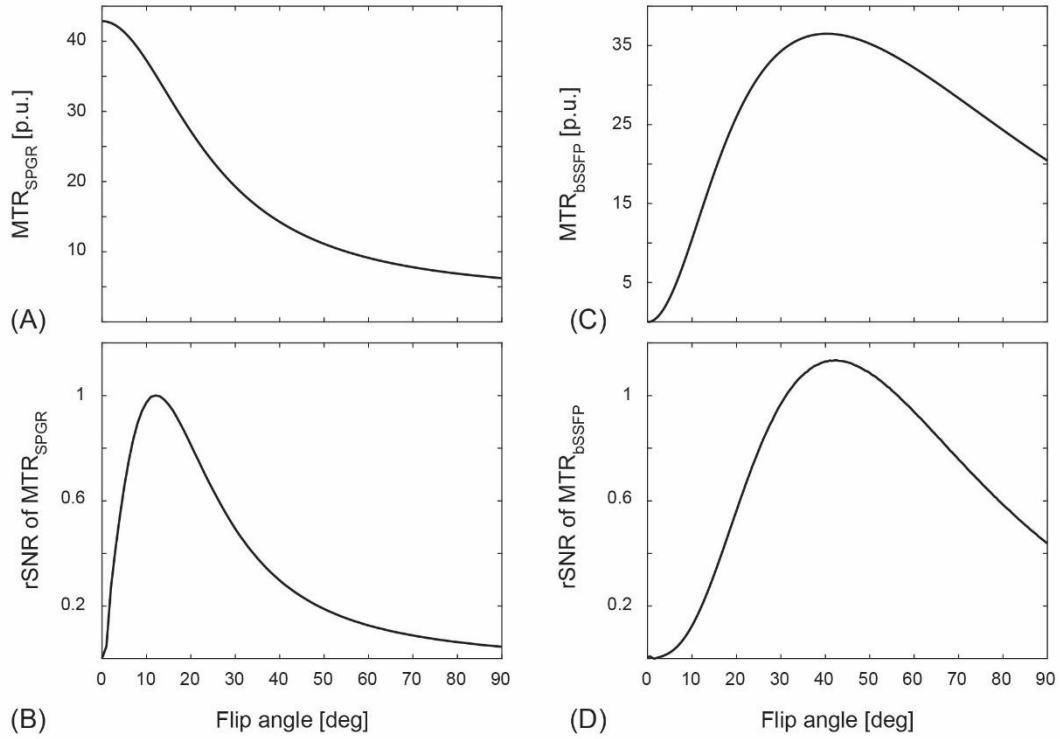

***Figure 2**: Simulated MTR and SNR of MTR as a function of flip angle for typical white matter values at 0.55 T using (A,B) SPGR and (C,D) bSSFP. The relative SNR (rSNR) values were derived by normalizing to the maximum SNR of MTR from SPGR.*

An estimate of the resulting MTR values and their corresponding SNR is given in Figure 5 as a function of the flip angle for brain white matter. For SPGR, MTR values increase with decreasing flip angles (Figure 5A) with a maximum SNR for a flip angle of 15° (Figure 5B); in agreement with simulations (see Figures 2A and 2B). Likewise, and in agreement with simulations (see Figures 2C and 2D), MTR values and SNR maximizes for bSSFP for a flip angle around 40° to 50° (Figure 5 C and 5D). In agreement with predictions, MTR imaging with bSSFP offers a slight increase in the SNR of about 13 %, as compared to SPGR at low field.

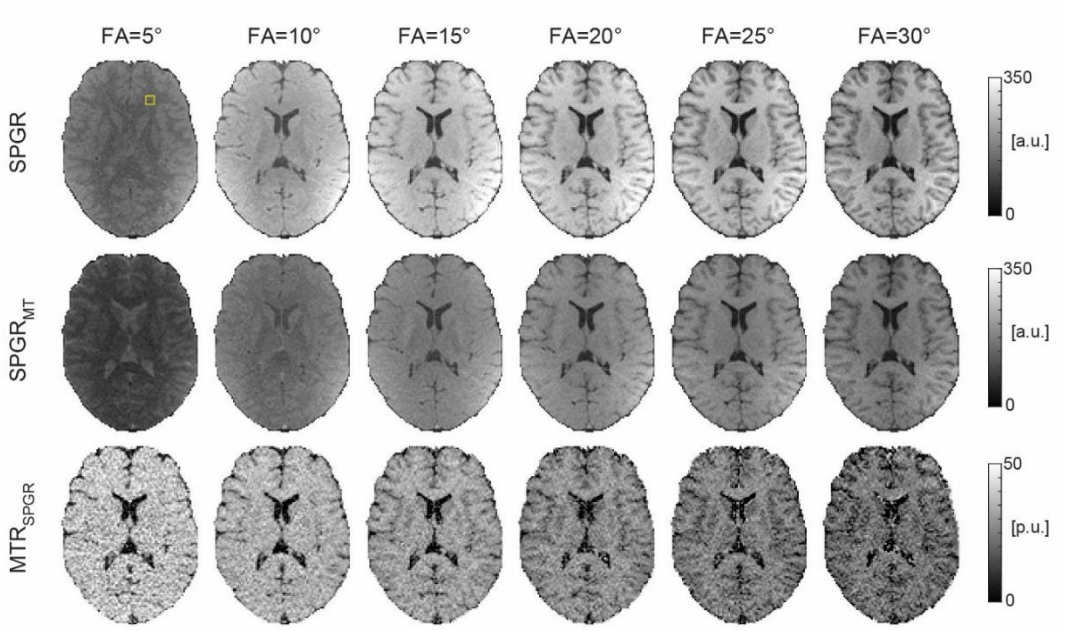

Figure 3: *From top to bottom: non-MT-weighted, MT-weighted, and MTR images produced by product SPGR sequence using different excitation flip angles. An exemplary ROI is shown on the top left image.*

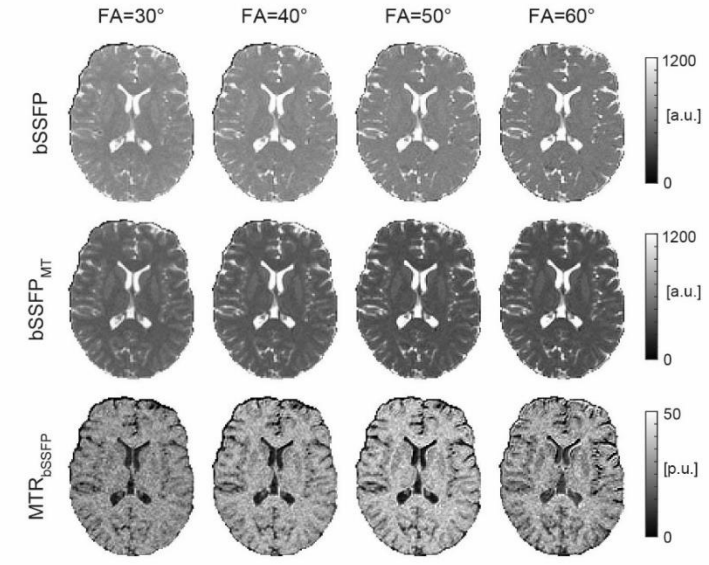

Figure 4: *From top to bottom: non-MT-weighted, MT-weighted, and MTR images produced by Cartesian bSSFP sequence at different excitation flip angles.*

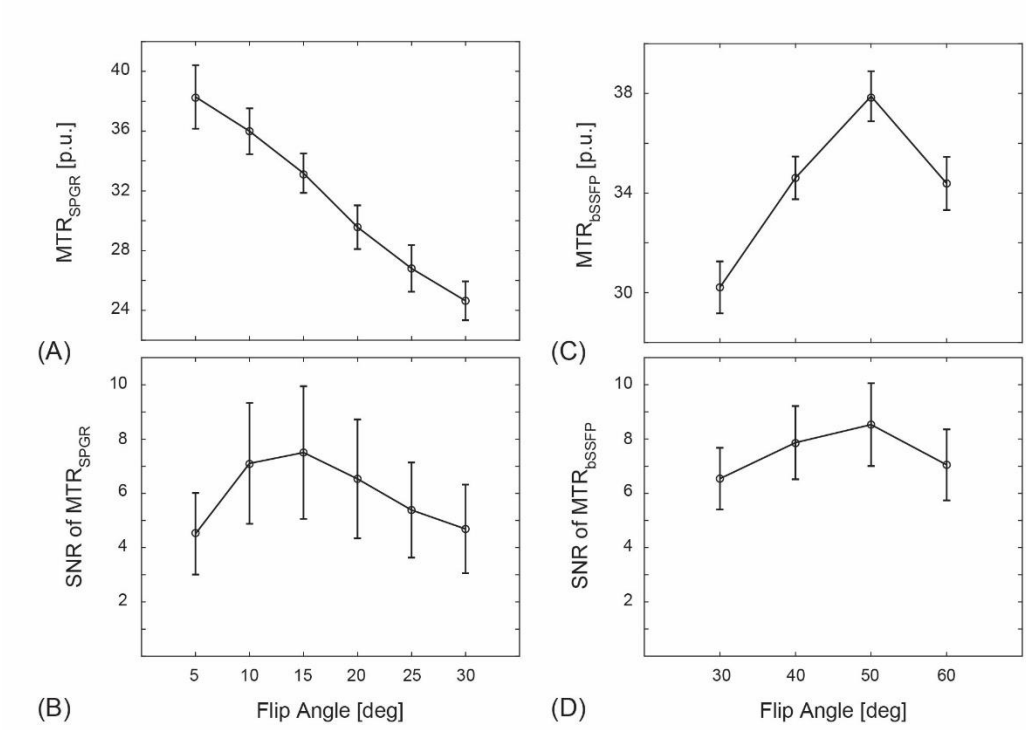

Figure 5: *Mean and standard deviation of MTR values obtained from ROIs in brain white matter along with their corresponding SNR, acquired with (A,B) SPGR and (C,D) bSSFP at 0.55 T. the average values are represented by circles, while the vertical lines indicate the standard deviation.*

In this study, however, Cartesian bSSFP imaging suffers from limited gradient switching times leading to a rather low sequence efficiency at low field as compared to what can be achieved on clinical state-of-the-art systems at high field. This results in an unnecessary drop in the overall SNR performance for bSSFP, as compared to SPGR imaging. The sequence efficiency of bSSFP can be considerably increased by using half-radial encoding, as proffered by bSTAR (see 'Methods' section). The prospects of bSSFP-MT brain imaging at low field are thus further explored with bSTAR using optimal MTR flip angle settings (see Figures 5C and 5D). The corresponding results are shown in Figure 6; reconstructed to the nominal isotropic resolution of 0.87 mm, as well as to lower resolutions of 1 mm and to 1.5 mm for direct visual comparison with the results from Cartesian bSSFP MTR imaging (Figure 4). Generally, the shortened TR with bSTAR, as compared to Cartesian bSSFP, results in an increase of the local average MTR value of frontal white matter from approximately 38 [p.u.] to about 46 [p.u.] due to increased saturation effects. For completeness, sagittal and coronal views of bSTAR-MTR imaging with nominal 0.87 mm isotropic resolution are shown in Figure 7. Observed MTR values were well within the typical expectation from high-field MT imaging (5,117).

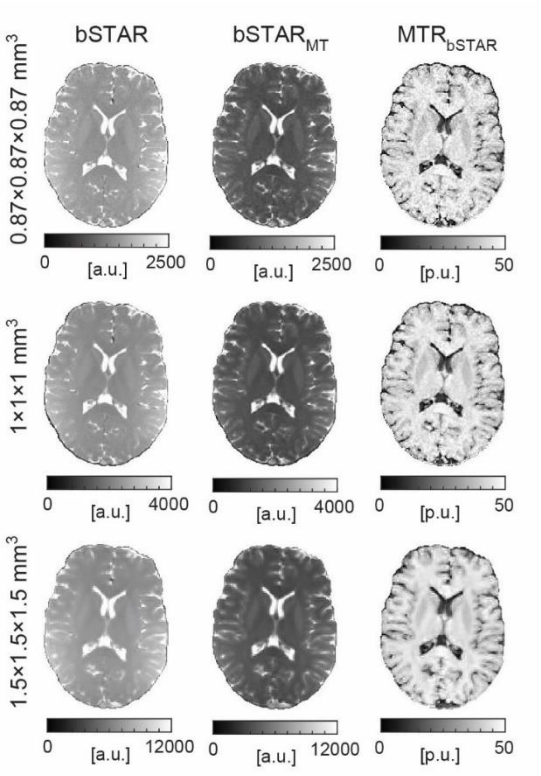

Figure 6: *From left to right: non-MT-weighted, MT-weighted, and MTR images produced by bSTAR sequence with flip angle of 40° and reconstructed with different resolutions.*

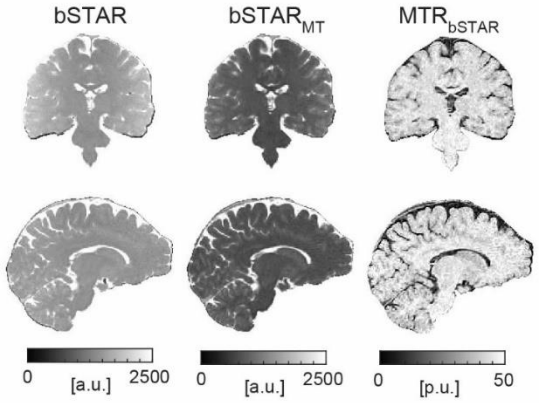

Figure 7: *Exemplary coronal and sagittal view of non-MT-weighted, MT-weighted, and MTR images from bSTAR sequence reconstructed with 0.87 mm resolution.*

Corresponding whole-brain, white and gray matter, MTR histograms are shown in Figure 8. The whole brain MTR histogram peak is located at 42.1 [p.u.] whereas white and gray matter peaks are located at 43.6 [p.u.] and 40.7 [p.u.]; respectively. The result of reproducibility assessment is summarized in Figure 9, showing the bulk white and gray matter histogram peak location values from 12 independent measurements (Figure 9A), as well as their mean and standard deviation (Figure 9B) for white matter (43.5 ± 0.08 [p.u.]) and gray matter (40.5 ± 0.2 [p.u.]).

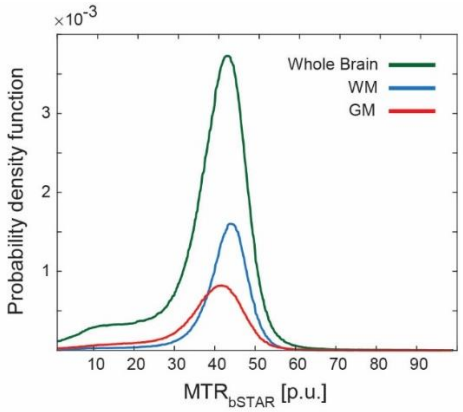

Figure 8: *MTR$_{bSTAR}$ histogram for whole brain (green line), segmented white matter (blue line) and segmented gray matter (red line) of a healthy subject. bSTAR images were reconstructed to 0.87 mm isotropic resolution. MTR values of CSF were removed from the histogram.*

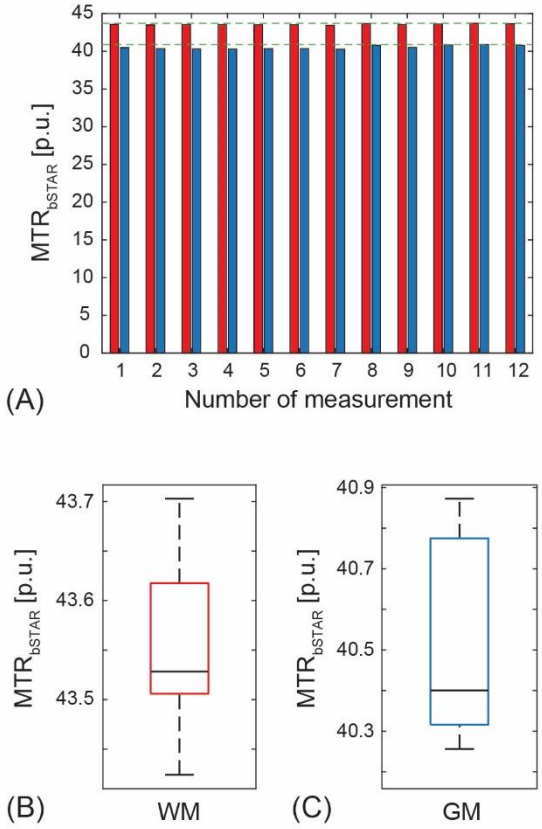

Figure 9: *Reproducibility assessment from scan–rescan experiments using an MTR histogram peak analysis of bSTAR images reconstructed offline with 0.87 mm isotropic resolution. (A) Histogram peak values of segmented WM (red) and segmented GM (blue) extracted from 12 repetitions. (B) corresponding box plots for WM and GM representing the median, lower and upper quartiles, as well as the maximum and minimum peak values.*

Discussion

At high field, MT imaging is commonly performed with SPGR using either 2D multi-slice (87) or 3D volumetric acquisitions (39). Generally, within the context of MT imaging, 2D multi-slice SPGR imaging offers a proton-weighted imaging base contrast, whereas 3D SPGR is typically T_1-weighted. MT imaging with bSSFP builds-up from a T_2/T_1-weighted image contrast. In this work, we compared 3D isotropic SPGR and bSSFP imaging for their prospects of MT imaging at low field. As shown by simulations, 3D SPGR imaging at low field results in a pronounced flip angle dependency in its steady state, as well as in the MTR, with rather diametral requirements: very low flip angles for maximum MTR values, but moderate flip angles close to the Ernst angle (118) to achieve a reasonable SNR for MTR imaging. This issue is of course also present at high field, but less accentuated as a result of the prolonged T_1 time with increasing main magnetic field (resulting in a decrease of the Ernst angle). Of course, also bSSFP shows some dependency on the field strength for MTR imaging, requiring higher flip angles for lower fields. For bSSFP, however, MTR maximizes around its optimal flip angles settings.

At low field, 3D MTR imaging of the brain with either SPGR or bSSFP offered an overall comparable SNR. For SPGR, a product sequence was used without further modification or optimization of the MT contrast; i.e., by optimizing the off-resonance irradiation frequency or the saturation power of the MT-

preparation pulses. For bSSFP, a custom sequence was used, offering a freely adjustable RF pulse duration. Since the RF pulse is used for both excitation and MT saturation, the flip angle cannot be adjusted freely to maximize the MT contrast. Typically, the flip angle is adjusted to the maximum bSSFP signal, and the MT contrast is optimized by minimizing the TR and the RF pulse duration for the MT-weighted bSSFP scan. This requirement, in combination with the low performance gradient system used in this work, resulted in a considerable drop in bSSFP's sequence efficiency, as compared to implementations on contemporary high-field systems. In order to bypass the issue of limited slew rates, a half-radial dual-echo bSSFP method, termed bSTAR, was used, offering maximum sequence efficiency. From the short TR, as proffered by bSTAR, MTR imaging of the brain at low field was essentially free of banding artifacts.

In combination with the compressed sensing reconstruction, bSTAR was able to provide MTR images of the brain down to sub-millimeter isotropic resolutions for acquisition times of less than 5 minutes. As a result, MTR brain imaging with bSTAR appears to be able to easily compete in terms of resolution and scan time with contemporary high-field MTR methods; offering unprecedented and rather unexpected performance for neurological examinations of the brain at low field. Its clinical value and sensitivity, however, still needs to be demonstrated and shown.

Conclusion

At low field, a half-radial double-echo bSSFP approach, termed bSTAR, in combination with a compressed sensing approach, offers sub-millimeter isotropic MTR imaging of the brain within comparable acquisition times to contemporary high-field imaging methods. MTR MRI of the brain with bSSFP thus offers excellent prospects for neurological examinations at low field; potentially without any noticeable limitations in terms of resolution and scan time due to the markedly reduced SNR at low field as compared to high field.

Chapter 5

Discussion, Outlook, and Conclusion

5.1 Discussion

The purpose of this thesis was to establish new imaging methodologies for rapid and robust MT imaging of the brain at both low (0.55 T) and high (3 T) field strength, with prospects for clinical routine application. At high fields, a spiral whole-brain MT-prepared SPGR technique was explored with regards to speed and accuracy. At low-fields, efficiency, and speed of a bSSFP-based technique (bSTAR) was expanded to sub-millimetre MT imaging of the brain. The main outcomes and shortcomings of these efforts are briefly described in the following:

Chapter 2. Current standard methods for MTR imaging on high-field MRI devices requires approximately 6 minutes of scanning time (87). To correct for B_1 non-uniformity, an additional B_1-map must be acquired, which can take between 1 to 10 minutes depending on the method used (73,75–77). In this chapter, a MT-prepared prototype interleaved 2D multi-slice SPGR sequence with spiral trajectory was combined with a low-resolution B_1-mapping acquisition to produce B_1-corrected MTR images in less than one minute. By encoding B_1 information within the same sequence scheme, B_1-correction could be achieved without incurring any extra scan time. Simulation results from the two-pool model for the specific TR and flip angle used in this study demonstrate that the B_1-related MTR variation in typical white matter and grey matter can be reduced by a factor of 10 when a simple first-order correction scheme is applied. Reproducibility assessments using the volumetric histogram peaks showed that B_1-correction reduced the scan-rescan variability of MTR. Overall, generated B_1-corrected MTR values were highly reproducible and in good agreement with previous work, offering potential for longitudinal studies.

It is important to note that the linear B_1-correction method used here is only suitable for PD-weighted images and may not be applicable when T_1-weighting of the MT-weighted signal cannot be ignored. In such cases, a nonlinear correction scheme may be necessary, which could increase the scan time. Furthermore, the speed of the proposed method in this study offers a reduced likelihood of motion-related artifacts between MT-weighted and non-MT-weighted images, however, some residual influence of non-matched motion states might still persist.

Chapter 3. Quantitative MT parameter estimation relies on the collection of multiple data points. To date, several qMT imaging methods have been proposed that take between 30 to 60 minutes (39–41,44). However, the lengthy acquisition time poses a challenge regarding their incorporation into clinical practice. The work presented here showed that highly accurate whole-brain B_1-corrected qMT parameter estimates can be obtained in less than 5 minutes using an MT-prepared interleaved multi-slice SPGR sequence similar to the one described in chapter 2. Numerical simulations confirmed suitability of a simple CW two-pool model in describing the data derived from the interleaved multi-slice scheme. An evaluation of 5 different sets of MT-weighted images consisting of 6 to 18 data points,

confirmed the stability of the proposed two-pool model. The results suggest B_1-correction is necessary, while B_0-related errors appear negligible.

The proposed rapid B_1-corrected qMT imaging method for 3 T is assumed to be faster than any previously reported method in the literature. However, it is important to keep the sampling scheme limited to off-resonances higher than 1 kHz to avoid direct saturation. This constraint enables further simplification of the two-pool model leading to reduced computational load but prevents exploration of low off-resonances. Furthermore, the sampling pattern for the series of acquired MT-weighted contrasts proposed in this work can further be optimized, potentially leading to an increase in accuracy of the qMT parameter estimates.

Chapter 4. MT imaging was previously performed at 0.5 T and 0.6 T field strengths almost three decades ago (6,40). However, due to the limited gradient efficiency at low fields, the resulting image resolution was poor, prompting the clinical MRI community to shift to higher fields for MT imaging. Nevertheless, with the recent re-introduction of clinical low-field MRI, new hardware and software advancements could improve MT imaging quality at low fields and thereby make it suitable for clinical applications. Here, a product SPGR sequence was compared to a MT-sensitized bSSFP.

Results from a comparison between commonly used MT-prepared SPGR and MT-sensitized bSSFP demonstrated that bSSFP slightly outperforms SPGR in terms of SNR, particularly at low fields, where reduced field inhomogeneities can ensure artifacts free bSSFP images. Furthermore, it was shown that the sequence efficiency of bSSFP can be improved considerably using a bSSFP-based method termed bSTAR, which utilizes a very high fraction of TR for signal sampling to achieve sub-millimeter MT images with higher SNR and increased MT sensitivity within the same scanning time as bSSFP. The bSTAR method was capable to provide MTR data at a nominal isotropic resolution of 0.87 mm.

5.2 Outlook

In this section an account of possible future work using the outcomes of this thesis is proposed.

Clinical environment: this thesis presents fast and robust MTR and qMT imaging approaches that enable further integration of MT parameter maps into clinical routine. Therefore, future work may focus on implementing the proposed methods into clinical practice. In this context, three areas can be explored: first, the fast and reliable MTR imaging methods proposed in chapters 2 and 4 are well-suited for longitudinal and multi-center studies. Therefore, it is important to develop a standard protocol aimed at achieving high inter-scanner reproducibility, similar to what has been done previously for MT-SPGR (87). Second, the qMT method proposed in chapter 3 provides reliable estimation of macromolecular proton fraction in brain tissue within a short acquisition time of 5 minutes. Although this parameter has demonstrated great potential in studying diseases such as MS and Alzheimer's due to its pathological

specificity (for a comprehensive review see (48)), its application has been limited by long acquisition times and complicated analysis pipelines, leading to a scarcity of trial studies and publications in this area. Therefore, it may be worthwhile to explore quantitative MT parameters as a complementary or alternative marker in studies related to the evolution and diagnosis of such diseases, using the method presented in this work. third, the submillimeter MTR imaging method proposed for low field systems in Chapter 4 has potential applications in high acuity brain imaging (119) for quickly identifying acute problems in patients in a cost-effective and safe manner, particularly when implants and metal objects are present. This technique could be incorporated into the emergency ward routine, e.g. for cases of stroke (120) or other traumatic brain injuries (121).

Optimized sampling pattern: The proposed qMT imaging pattern can be further optimized to decrease uncertainty in the MT parameter estimates. Perhaps an iterative reduction approach as reported in ref. (94) or a Cramer Rao Lower Bound method as suggested in ref. (97) could be adapted to our proposed qMT imaging technique. To which extent each of the quantitative parameter maps will benefit from the optimized sampling scheme is yet to be determined.

qMT at low-fields: At low-field strengths, sub-millimeter MTR maps of the brain have been obtained with bSTAR imaging. Since MTR is a semi-quantitative rather than a fully quantitative measure, a natural extension of this method will be the extraction of the qMT parameters to further enhance the great potential of bSTAR in the field of MT imaging for clinical applications. To this end, a previously proposed qMT bSSFP two-pool model (44) can be adjusted to our application to provide quantitative MT estimates and thus a more objective tissue characterization as compared to MTR . The limitations and potential of this method in modeling the bSTAR MT data at low fields is still subject to research.

Deep learning: In this thesis, we addressed the lengthy acquisition time required for qMT imaging. As a continuation of this work, the post-acquisition time required for voxel-by-voxel two-pool model fitting can be reduced by using an artificial neural network (ANN)-based method as it was used for MR fingerprinting (122) or diffusion MRI (123). Deep learning, an ANN-based approach, can reduce the post-processing time for two-pool model fitting. Recently, such an approach was applied to accelerate qMT model fitting (124), and it can be employed in conjunction with the method developed in chapter three to further enhance the efficiency of the proposed framework.

5.3 Conclusion

In conclusion, this thesis successfully addressed some of the current challenges of MT imaging by developing rapid and robust approaches in both high and low fields. At low field, the efficiency of the proposed acquisition scheme was leveraged to achieve MTR maps of submillimeter resolution within 5 minutes. At high field, the speed of the spiral acquisition was invested to obtain reliable B_1-corrected

MTR maps in only one minute and fully quantitative B_1-corrected MT parameter maps in only five minutes. Overall, the proposed methods promote practicality of MT imaging in clinical settings.

References

1. Wolff SD, Balaban RS. Magnetization transfer contrast (MTC) and tissue water proton relaxation in vivo. Magn Reson Med. 1989;10(1):135–44.

2. Horsfield MA. Magnetization Transfer Imaging in Multiple Sclerosis. J Neuroimaging. 2005;15(s4):58S-67S.

3. Henkelman RM, Stanisz GJ, Graham SJ. Magnetization transfer in MRI: a review. NMR Biomed. 2001;14(2):57–64.

4. Barker GJ, Tofts PS, Gass A. An interleaved sequence for accurate and reproducible clinical measurement of Magnetization Transfer Ratio. Magn Reson Imaging. 1996 Jan 1;14(4):403–11.

5. Dousset V, Grossman RI, Ramer KN, Schnall MD, Young LH, Gonzalez-Scarano F, et al. Experimental allergic encephalomyelitis and multiple sclerosis: lesion characterization with magnetization transfer imaging. Radiology. 1992 Feb;182(2):483–91.

6. Henkelman RM, Huang X, Xiang QS, Stanisz GJ, Swanson SD, Bronskill MJ. Quantitative interpretation of magnetization transfer. Magn Reson Med. 1993 Jun;29(6):759–66.

7. Pike GB. Pulsed magnetization transfer contrast in gradient echo imaging: A two-pool analytic description of signal response. Magn Reson Med. 1996;36(1):95–103.

8. Hu BS, Conolly SM, Wright GA, Nishimura DG, Macovski A. Pulsed saturation transfer contrast. Magn Reson Med. 1992;26(2):231–40.

9. Pike GB, Glover GH, Hu BS, Enzmann DR. Pulsed magnetization transfer spin-echo MR imaging. J Magn Reson Imaging. 1993;3(3):531–9.

10. Schneider E, Prost RW, Glover GH. Pulsed magnetization transfer versus continuous wave irradiation for tissue contrast enhancement. J Magn Reson Imaging. 1993;3(2):417–23.

11. Wolff SD, Balaban RS. Magnetization transfer imaging: practical aspects and clinical applications. Radiology. 1994 Sep 1;192(3):593–9.

12. Hua J, Hurst GC. Analysis of on- and off-resonance magnetization transfer techniques. J Magn Reson Imaging JMRI. 1995 Feb;5(1):113–20.

13. Helms G, Frahm J. Magnetization transfer attenuation of creatine resonances in localized proton MRS of human brain in vivo. NMR Biomed. 1999;12(8):490–4.

14. Battiston M, Schneider T, Grussu F, Yiannakas MC, Prados F, De Angelis F, et al. Fast bound pool fraction mapping via steady-state magnetization transfer saturation using single-shot EPI. Magn Reson Med. 2019;82(3):1025–40.

15. Gass A, Barker GJ, Kidd D, Thorpe JW, MacManus D, Brennan A, et al. Correlation of magnetization transfer ration with clinical disability in multiple sclerosis. Ann Neurol. 1994;36(1):62–7.

16. Bieri O, Scheffler K. On the origin of apparent low tissue signals in balanced SSFP. Magn Reson Med. 2006;56(5):1067–74.

17. Bieri O, Scheffler K. Optimized balanced steady-state free precession magnetization transfer imaging. Magn Reson Med. 2007;58(3):511–8.

18. Forsén S, Hoffman RA. Study of Moderately Rapid Chemical Exchange Reactions by Means of Nuclear Magnetic Double Resonance. J Chem Phys. 1963 Dec 1;39(11):2892–901.

19. Eng J, Ceckler TL, Balaban RS. Quantitative 1H magnetization transfer imaging in vivo. Magn Reson Med. 1991;17(2):304–14.

20. Pui MH. Magnetization transfer analysis of brain tumor, infection, and infarction. J Magn Reson Imaging. 2000;12(3):395–9.

21. Okumura A, Takenaka K, Nishimura Y, Asano Y, Sakai N, Kuwata K, et al. The characterization of human brain tumor using magnetization transfer technique in magnetic resonance imaging. Neurol Res. 1999 Apr 1;21(3):250–4.

22. Hanyu H, Asano T, Sakurai H, Takasaki M, Shindo H, Abe K. Magnetization transfer measurements of the hippocampus in the early diagnosis of Alzheimer's disease. J Neurol Sci. 2001 Jul 15;188(1):79–84.

23. Fornari E, Maeder P, Meuli R, Ghika J, Knyazeva MG. Demyelination of superficial white matter in early Alzheimer's disease: a magnetization transfer imaging study. Neurobiol Aging. 2012 Feb 1;33(2):428.e7-428.e19.

24. Schmierer K, Scaravilli F, Altmann DR, Barker GJ, Miller DH. Magnetization transfer ratio and myelin in postmortem multiple sclerosis brain. Ann Neurol. 2004;56(3):407–15.

25. Moccia M, Pavert S van de, Eshaghi A, Haider L, Pichat J, Yiannakas M, et al. Pathologic correlates of the magnetization transfer ratio in multiple sclerosis. Neurology. 2020 Dec 1;95(22):e2965–76.

26. Grossman RI. Magnetization transfer in multiple sclerosis. Ann Neurol. 1994;36(S1):S97–9.

27. Hu H, Chen L, Zhou J, Chen W, Chen HH, Zhang JL, et al. Multiparametric magnetic resonance imaging for differentiating active from inactive thyroid-associated ophthalmopathy: Added value from magnetization transfer imaging. Eur J Radiol. 2022 Jun 1;151:110295.

28. Yousem DM, Montone KT, Sheppard LM, Rao VM, Weinstein GS, Hayden RE. Head and neck neoplasms: magnetization transfer analysis. Radiology. 1994 Sep;192(3):703–7.

29. Martens MH, Lambregts DMJ, Papanikolaou N, Heijnen LA, Riedl RG, zur Hausen A, et al. Magnetization Transfer Ratio: A Potential Biomarker for the Assessment of Postradiation Fibrosis in Patients With Rectal Cancer. Invest Radiol. 2014 Jan;49(1):29.

30. Barrett T, McLean M, Priest AN, Lawrence EM, Patterson AJ, Koo BC, et al. Diagnostic evaluation of magnetization transfer and diffusion kurtosis imaging for prostate cancer detection in a re-biopsy population. Eur Radiol. 2018 Aug 1;28(8):3141–50.

31. Virostko J, Sorace AG, Wu C, Ekrut D, Jarrett AM, Upadhyaya RM, et al. Magnetization Transfer MRI of Breast Cancer in the Community Setting: Reproducibility and Preliminary Results in Neoadjuvant Therapy. Tomography. 2019 Mar;5(1):44–52.

32. Buchem MA van, McGowan JC, Kolson DL, Polansky M, Grossman RI. Quantitative volumetric magnetization transfer analysis in multiple sclerosis: Estimation of macroscopic and microscopic disease burden. Magn Reson Med. 1996;36(4):632–6.

33. Ropele S, Fazekas F. Magnetization transfer MR imaging in multiple sclerosis. Neuroimaging Clin N Am. 2009 Feb;19(1):27–36.

34. Tortorella C, Viti B, Bozzali M, Sormani MP, Rizzo G, Gilardi MF, et al. A magnetization transfer histogram study of normal-appearing brain tissue in MS. Neurology. 2000 Jan 11;54(1):186–186.

35. Ge Y, Grossman RI, Udupa JK, Babb JS, Kolson DL, McGowan JC. Magnetization Transfer Ratio Histogram Analysis of Gray Matter in Relapsing-remitting Multiple Sclerosis. Am J Neuroradiol. 2001 Mar 1;22(3):470–5.

36. McConnell HM. Reaction Rates by Nuclear Magnetic Resonance. J Chem Phys. 1958 Mar;28(3):430–1.

37. Morrison C, Henkelman RM. A Model for Magnetization Transfer in Tissues. Magn Reson Med. 1995;33(4):475–82.

38. Yarnykh VL. Fast macromolecular proton fraction mapping from a single off-resonance magnetization transfer measurement. Magn Reson Med. 2012;68(1):166–78.

39. Sled JG, Pike GB. Quantitative interpretation of magnetization transfer in spoiled gradient echo MRI sequences. J Magn Reson. 2000 Jul;145(1):24–36.

40. Yarnykh VL. Pulsed Z-spectroscopic imaging of cross-relaxation parameters in tissues for human MRI: Theory and clinical applications. Magn Reson Med. 2002;47(5):929–39.

41. Ramani A, Dalton C, Miller DH, Tofts PS, Barker GJ. Precise estimate of fundamental in-vivo MT parameters in human brain in clinically feasible times. Magn Reson Imaging. 2002 Dec 1;20(10):721–31.

42. Portnoy S, Stanisz GJ. Modeling pulsed magnetization transfer. Magn Reson Med. 2007;58(1):144–55.

43. Cercignani M, Barker GJ. A comparison between equations describing in vivo MT: The effects of noise and sequence parameters. J Magn Reson. 2008 Apr;191(2):171–83.

44. Gloor M, Scheffler K, Bieri O. Quantitative magnetization transfer imaging using balanced SSFP. Magn Reson Med. 2008 Sep;60(3):691–700.

45. Lazari A, Lipp I. Can MRI measure myelin? Systematic review, qualitative assessment, and meta-analysis of studies validating microstructural imaging with myelin histology. NeuroImage. 2021 Apr 15;230:117744.

46. Khodanovich MY, Sorokina IV, Glazacheva VY, Akulov AE, Nemirovich-Danchenko NM, Romashchenko AV, et al. Histological validation of fast macromolecular proton fraction mapping as a quantitative myelin imaging method in the cuprizone demyelination model. Sci Rep. 2017 Apr 24;7:46686.

47. (ISMRM 2020) Macromolecular proton fraction as a marker of myelin recovery in ischemic stroke [Internet]. [cited 2023 Apr 4]. Available from: https://archive.ismrm.org/2020/1923.html

48. Kisel AA, Naumova AV, Yarnykh VL. Macromolecular Proton Fraction as a Myelin Biomarker: Principles, Validation, and Applications. Front Neurosci. 2022 Feb 9;16:819912.

49. Schmierer K, Tozer DJ, Scaravilli F, Altmann DR, Barker GJ, Tofts PS, et al. Quantitative magnetization transfer imaging in postmortem multiple sclerosis brain. J Magn Reson Imaging. 2007;26(1):41–51.

50. Yarnykh VL, Bowen JD, Samsonov A, Repovic P, Mayadev A, Qian P, et al. Fast Whole-Brain Three-dimensional Macromolecular Proton Fraction Mapping in Multiple Sclerosis. Radiology. 2015 Jan;274(1):210–20.

51. Harrison NA, Cooper E, Dowell NG, Keramida G, Voon V, Critchley HD, et al. Quantitative Magnetization Transfer Imaging as a Biomarker for Effects of Systemic Inflammation on the Brain. Biol Psychiatry. 2015 Jul 1;78(1):49–57.

52. Marques JP, Simonis FFJ, Webb AG. Low-field MRI: An MR physics perspective. J Magn Reson Imaging. 2019;49(6):1528–42.

53. Anisimov NV, Pavlova OS, Pirogov YA, Yarnykh VL. Three-dimensional fast single-point macromolecular proton fraction mapping of the human brain at 0.5 Tesla. Quant Imaging Med Surg. 2020 Jul;10(7):1441–9.

54. Tofts PS, Steens SCA, Cercignani M, Admiraal-Behloul F, Hofman PAM, van Osch MJP, et al. Sources of variation in multi-centre brain MTR histogram studies: body-coil transmission eliminates inter-centre differences. Magn Reson Mater Phys Biol Med. 2006 Sep 1;19(4):209–22.

55. York EN, Thrippleton MJ, Meijboom R, Hunt DPJ, Waldman AD. Quantitative magnetization transfer imaging in relapsing-remitting multiple sclerosis: a systematic review and meta-analysis. Brain Commun. 2022 Apr 1;4(2):fcac088.

56. Boudreau M, Stikov N, Pike GB. B1-sensitivity analysis of quantitative magnetization transfer imaging. Magn Reson Med. 2018;79(1):276–85.

57. Bagnato F. Chapter 26 - Clinical application of magnetization transfer imaging. In: Choi IY, Jezzard P, editors. Advances in Magnetic Resonance Technology and Applications [Internet]. Academic Press; 2021 [cited 2023 Apr 4]. p. 403–17. (Advanced Neuro MR Techniques and Applications; vol. 4). Available from: https://www.sciencedirect.com/science/article/pii/B9780128224793000415

58. Paul Tofts. Quantitative MRI of the Brain: Measuring Changes Caused by Disease. 2004. 650 p.

59. Buchem MA van, Steens SCA, Vrooman HA, Zwinderman AH, McGowan JC, Rassek M, et al. Global Estimation of Myelination in the Developing Brain on the Basis of Magnetization Transfer Imaging: A Preliminary Study. Am J Neuroradiol. 2001 Apr 1;22(4):762–6.

60. Spilt A, Geeraedts T, Craen AJM de, Westendorp RGJ, Blauw GJ, Buchem MA van. Age-Related Changes in Normal-Appearing Brain Tissue and White Matter Hyperintensities: More of the Same or Something Else? Am J Neuroradiol. 2005 Apr 1;26(4):725–9.

61. Waesberghe JHTMV, Kamphorst W, Groot CJAD, Walderveen MAAV, Castelijns JA, Ravid R, et al. Axonal loss in multiple sclerosis lesions: Magnetic resonance imaging insights into substrates of disability. Ann Neurol. 1999;46(5):747–54.

62. Barbosa S, Blumhardt LD, Roberts N, Lock T, Edwards RHT. Magnetic resonance relaxation time mapping in multiple sclerosis: Normal appearing white matter and the “invisible” lesion load. Magn Reson Imaging. 1994 Jan 1;12(1):33–42.

63. Filippi M, Campi A, Dousset V, Baratti C, Martinelli V, Canal N, et al. A Magnetization Transfer Imaging Study of Normal-Appearing White Matter in Multiple Sclerosis. Neurology. 1995 Mar 1;45(3):478.

64. Loevner LA, Grossman RI, Cohen JA, Lexa FJ, Kessler D, Kolson DL. Microscopic disease in normal-appearing white matter on conventional MR images in patients with multiple sclerosis: assessment with magnetization-transfer measurements. Radiology. 1995 Aug 1;196(2):511–5.

65. Flier WMVD, Heuvel DMJVD, Weverling-Rijnsburger AWE, Bollen ELEM, Westendorp RGJ, Buchem MAV, et al. Magnetization transfer imaging in normal aging, mild cognitive impairment, and Alzheimer’s disease. Ann Neurol. 2002;52(1):62–7.

66. Buchem MA van, Udupa JK, McGowan JC, Miki Y, Heyning FH, Boncoeur-Martel MP, et al. Global volumetric estimation of disease burden in multiple sclerosis based on magnetization transfer imaging. Am J Neuroradiol. 1997 Aug 1;18(7):1287–90.

67. Kalkers NF, Hintzen RQ, van Waesberghe JHTM, Lazeron RHC, van Schijndel RA, Adèr HJ, et al. Magnetization transfer histogram parameters reflect all dimensions of MS pathology, including atrophy. J Neurol Sci. 2001 Mar 1;184(2):155–62.

68. Filippi M, Iannucci G, Tortorella C, Minicucci L, Horsfield MA, Colombo B, et al. Comparison of MS clinical phenotypes using conventional and magnetization transfer MRI. Neurology. 1999 Feb 1;52(3):588.

69. Davies GR, Ramió-Torrentà L, Hadjiprocopis A, Chard DT, Griffin CMB, Rashid W, et al. Evidence for grey matter MTR abnormality in minimally disabled patients with early relapsing-remitting multiple sclerosis. J Neurol Neurosurg Amp Psychiatry. 2004 Jul 1;75(7):998.

70. Ge Y, Grossman RI, Babb JS, Rabin ML, Mannon LJ, Kolson DL. Age-related total gray matter and white matter changes in normal adult brain. Part II: quantitative magnetization transfer ratio histogram analysis. AJNR Am J Neuroradiol. 2002 Sep;23(8):1334–41.

71. Graham SJ, Henkelman RM. Understanding pulsed magnetization transfer. J Magn Reson Imaging. 1997;7(5):903–12.

72. Pike GB, Glover GH, Hu BS, Enzmann DR. Pulsed magnetization transfer spin-echo MR imaging. J Magn Reson Imaging. 1993;3(3):531–9.

73. Ropele S, Filippi M, Valsasina P, Korteweg T, Barkhof F, Tofts PS, et al. Assessment and correction of B1-induced errors in magnetization transfer ratio measurements. Magn Reson Med. 2005;53(1):134–40.

74. Helms G, Dathe H, Dechent P. Modeling the influence of TR and excitation flip angle on the magnetization transfer ratio (MTR) in human brain obtained from 3D spoiled gradient echo MRI. Magn Reson Med. 2010;64(1):177–85.

75. Volz S, Nöth U, Rotarska-Jagiela A, Deichmann R. A fast B1-mapping method for the correction and normalization of magnetization transfer ratio maps at 3 T. NeuroImage. 2010 Feb 15;49(4):3015–26.

76. Samson RS, Wheeler-Kingshott CAM, Symms MR, Tozer DJ, Tofts PS. A simple correction for B1 field errors in magnetization transfer ratio measurements. Magn Reson Imaging. 2006 Apr;24(3):255–63.

77. Yarnykh VL, Khodanovich MYu. Analytical Method of Correction of B1 Errors in Mapping of Magnetization Transfer Ratio in Highfield Magnetic Resonance Tomography. Russ Phys J. 2015 Apr 1;57(12):1784–8.

78. Ma D, Gulani V, Seiberlich N, Liu K, Sunshine JL, Duerk JL, et al. Magnetic resonance fingerprinting. Nature. 2013 Mar;495(7440):187–92.

79. Heule R, Pfeuffer J, Meyer CH, Bieri O. Simultaneous B1 and T1 mapping using spiral multislice variable flip angle acquisitions for whole-brain coverage in less than one minute. Magn Reson Med. 2019;81(3):1876–89.

80. Meyer CH, Zhao L, Lustig M, Jilwan-Nicolas M, Wintermark M, Iii JPM, et al. Dual-Density and Parallel Spiral ASL for Motion Artifact Reduction. Proc Intl Soc Magn Reson Med. 2011;19:3986.

81. Heule R, Pfeuffer J, Bieri O. Snapshot whole-brain T1 relaxometry using steady-state prepared spiral multislice variable flip angle imaging. Magn Reson Med. 2018;79(2):856–66.

82. Tan H, Meyer CH. Estimation of k-space trajectories in spiral MRI. Magn Reson Med. 2009;61(6):1396–404.

83. Mugler III JP, Brookeman JR. Rapid three-dimensional T1-weighted MR imaging with the MP-RAGE sequence. J Magn Reson Imaging. 1991;1(5):561–7.

84. Lustig M, Pauly JM. SPIRiT: Iterative self-consistent parallel imaging reconstruction from arbitrary k-space. Magn Reson Med. 2010;64(2):457–71.

85. Stollberger R, Wach P. Imaging of the active B1 field in vivo. Magn Reson Med. 1996;35(2):246–51.

86. Ganter C. Configuration Model. In: Proc Intl Soc Mag Reson Med 26. France; 2018. p. 5663.

87. Barker GJ, Schreiber WG, Gass A, Ranjeva JP, Campi A, Waesberghe JHTM van, et al. A standardised method for measuring magnetisation transfer ratio on MR imagers from different manufacturers—the EuroMT sequence. Magn Reson Mater Phys Biol Med. 2005 May 1;18(2):76–80.

88. Bozzali M, Franceschi M, Falini A, Pontesilli S, Cercignani M, Magnani G, et al. Quantification of tissue damage in AD using diffusion tensor and magnetization transfer MRI. Neurology. 2001 Sep 25;57(6):1135.

89. Kabani NJ, Sled JG, Chertkow H. Magnetization Transfer Ratio in Mild Cognitive Impairment and Dementia of Alzheimer's Type. NeuroImage. 2002 Mar 1;15(3):604–10.

90. Samsonov A, Alexander AL, Mossahebi P, Wu YC, Duncan ID, Field AS. Quantitative MR imaging of two-pool magnetization transfer model parameters in myelin mutant shaking pup. NeuroImage. 2012 Sep 1;62(3):1390–8.

91. Yarnykh VL. Time-efficient, high-resolution, whole brain three-dimensional macromolecular proton fraction mapping. Magn Reson Med. 2016;75(5):2100–6.

92. Afshari R, Santini F, Heule R, Meyer CH, Pfeuffer J, Bieri O. One-minute whole-brain magnetization transfer ratio imaging with intrinsic B1-correction. Magn Reson Med. 2021;85(5):2686–95.

93. Heule R, Bieri O. Rapid and robust variable flip angle T1 mapping using interleaved two-dimensional multislice spoiled gradient echo imaging. Magn Reson Med. 2017;77(4):1606–11.

94. Levesque IR, Sled JG, Pike GB. Iterative optimization method for design of quantitative magnetization transfer imaging experiments. Magn Reson Med. 2011;66(3):635–43.

95. Sled JG, Pike GB. Quantitative imaging of magnetization transfer exchange and relaxation properties in vivo using MRI. Magn Reson Med. 2001;46(5):923–31.

96. Sled J g., Levesque I, Santos A c., Francis S j., Narayanan S, Brass S d., et al. Regional variations in normal brain shown by quantitative magnetization transfer imaging. Magn Reson Med. 2004;51(2):299–303.

97. Cercignani M, Alexander DC. Optimal acquisition schemes for in vivo quantitative magnetization transfer MRI. Magn Reson Med. 2006 Oct;56(4):803–10.

98. Boudreau M, Pike GB. Sensitivity regularization of the Cramér-Rao lower bound to minimize B1 nonuniformity effects in quantitative magnetization transfer imaging. Magn Reson Med. 2018;80(6):2560–72.

99. Ridha BH, Symms MR, Tozer DJ, Stockton KC, Frost C, Siddique MM, et al. Magnetization Transfer Ratio in Alzheimer Disease: Comparison with Volumetric Measurements. Am J Neuroradiol. 2007 May 1;28(5):965–70.

100. Chen JTH, Easley K, Schneider C, Nakamura K, Kidd GJ, Chang A, et al. Clinically feasible MTR is sensitive to cortical demyelination in MS. Neurology. 2013 Jan 15;80(3):246–52.

101. Granziera C, Wuerfel J, Barkhof F, Calabrese M, De Stefano N, Enzinger C, et al. Quantitative magnetic resonance imaging towards clinical application in multiple sclerosis. Brain. 2021 May 1;144(5):1296–311.

102. Tang X, Zhang H, Zhou J, Kang H, Yang S, Cui H, et al. Brain development in children with developmental delay using amide proton transfer-weighted imaging and magnetization transfer imaging. Pediatr Investig. 2020 Dec;04(04):250–6.

103. Dubois J, Dehaene-Lambertz G, Kulikova S, Poupon C, Hüppi PS, Hertz-Pannier L. The early development of brain white matter: A review of imaging studies in fetuses, newborns and infants. Neuroscience. 2014 Sep 12;276:48–71.

104. Amann M, Sprenger T, Naegelin Y, Reinhardt J, Kuster P, Hirsch JG, et al. Comparison between balanced steady-state free precession and standard spoiled gradient echo magnetization transfer ratio imaging in multiple sclerosis: methodical and clinical considerations. NeuroImage. 2015 Mar 1;108:87–94.

105. Bieri O, Scheffler K. Fundamentals of balanced steady state free precession MRI. J Magn Reson Imaging. 2013;38(1):2–11.

106. Tian Y, Cui SX, Lim Y, Lee NG, Zhao Z, Nayak KS. Contrast-optimal simultaneous multi-slice bSSFP cine cardiac imaging at 0.55 T. Magn Reson Med. 2023 Feb;89(2):746–55.

107. Ponrartana S, Nguyen HN, Cui SX, Tian Y, Kumar P, Wood JC, et al. Low-field 0.55 T MRI evaluation of the fetus. Pediatr Radiol. 2023 Mar 8;

108. Azour L, Condos R, Keerthivasan MB, Bruno M, Pandit Sood T, Landini N, et al. Low-field 0.55 T MRI for assessment of pulmonary groundglass and fibrosis-like opacities: Inter-reader and inter-modality concordance. Eur J Radiol. 2022 Nov 1;156:110515.

109. Iyyakkunnel S, Bieri O. Conductivity mapping at 0.55 T with balanced steady state free precession. In London; 2022.

110. Campbell-Washburn AE, Jiang Y, Körzdörfer G, Nittka M, Griswold MA. Feasibility of MR fingerprinting using a high-performance 0.55 T MRI system. Magn Reson Imaging. 2021 Sep;81:88–93.

111. Campbell-Washburn AE, Ramasawmy R, Restivo MC, Bhattacharya I, Basar B, Herzka DA, et al. Opportunities in Interventional and Diagnostic Imaging by Using High-Performance Low-Field-Strength MRI. Radiology. 2019 Nov;293(2):384–93.

112. Bauman G, Bieri O. Balanced steady-state free precession thoracic imaging with half-radial dual-echo readout on smoothly interleaved archimedean spirals. Magn Reson Med. 2020 Jul;84(1):237–46.

113. Beck A, Teboulle M. A Fast Iterative Shrinkage-Thresholding Algorithm for Linear Inverse Problems. SIAM J Imaging Sci. 2009 Jan 1;2(1):183–202.

114. Dietrich O, Raya JG, Reeder SB, Reiser MF, Schoenberg SO. Measurement of signal-to-noise ratios in MR images: influence of multichannel coils, parallel imaging, and reconstruction filters. J Magn Reson Imaging JMRI. 2007 Aug;26(2):375–85.

115. Heule R, Bär P, Mirkes C, Scheffler K, Trattnig S, Bieri O. Triple-echo steady-state T2 relaxometry of the human brain at high to ultra-high fields. NMR Biomed. 2014 Sep;27(9):1037–45.

116. Heule R, Pfeuffer J, Meyer CH, Bieri O. Simultaneous B1 and T1 mapping using spiral multislice variable flip angle acquisitions for whole-brain coverage in less than one minute. Magn Reson Med. 2019;81(3):1876–89.

117. Smith SA, Farrell JAD, Jones CK, Reich DS, Calabresi PA, van Zijl PCM. Pulsed magnetization transfer imaging with body coil transmission at 3 Tesla: Feasibility and application. Magn Reson Med. 2006;56(4):866–75.

118. Markl M, Leupold J. Gradient echo imaging. J Magn Reson Imaging. 2012;35(6):1274–89.

119. Arnold TC, Freeman CW, Litt B, Stein JM. Low-field MRI: Clinical promise and challenges. J Magn Reson Imaging. 2023;57(1):25–44.

120. Pendleburyab ST, Lee MA, Blamire AM, Styles P, Matthews PM. Correlating magnetic resonance imaging markers of axonal injury and demyelination in motor impairment secondary to stroke and multiple sclerosis. Magn Reson Imaging. 2000 May 1;18(4):369–78.

121. Wilde EA, Wanner IB, Kenney K, Gill J, Stone JR, Disner S, et al. A Framework to Advance Biomarker Development in the Diagnosis, Outcome Prediction, and Treatment of Traumatic Brain Injury. J Neurotrauma. 2022 Apr;39(7–8):436–57.

122. Cohen O, Zhu B, Rosen MS. MR fingerprinting Deep RecOnstruction NEtwork (DRONE). Magn Reson Med. 2018 Sep;80(3):885–94.

123. Gyori NG, Palombo M, Clark CA, Zhang H, Alexander DC. Training data distribution significantly impacts the estimation of tissue microstructure with machine learning. Magn Reson Med. 2022 Feb;87(2):932–47.

124. Luu HM, Kim DH, Kim JW, Choi SH, Park SH. qMTNet: Accelerated quantitative magnetization transfer imaging with artificial neural networks. Magn Reson Med. 2021;85(1):298–308.